Title: Production Through Simulation: Using Simulation Technologies to Create and Evaluate Nuclear Fuel Fabrication Facility Designs

Author(s): Bourque, Cade Michael

Intended for: Thesis published in fulfillment of MS degree

Issued: 2021-07-12

The Thesis Committee for Cade Michael Bourque
Certifies that this is the approved version of the following Thesis:

Production Through Simulation: Using Simulation Technologies to Create and Evaluate Nuclear Fuel Fabrication Facility Designs

APPROVED BY

SUPERVISING COMMITTEE:

Kevin T. Clarno, Supervisor

Benjamin D. Leibowicz, Co-Supervisor

Production Through Simulation: Using Simulation Technologies to Create and Evaluate Nuclear Fuel Fabrication Facility Designs

by

Cade Michael Bourque, B.S.

Thesis

Presented to the Faculty of the Graduate School of

The University of Texas at Austin

in Partial Fulfillment

of the Requirements

for the Degree of

Masters of Science in Mechanical Engineering

The University of Texas at Austin
December 2020

Dedication

To my parents, Dreux and Dianne, for their unwavering support and encouragement;

And to my best friends, Semper and Cosmo – good boys.

Acknowledgements

Abstract

Production Through Simulation: Using Simulation Technologies to Create and Evaluate Nuclear Fuel Fabrication Facility Designs

Cade Michael Bourque, M.S.M.E.

The University of Texas at Austin, 2020

Supervisor: Kevin T. Clarno, Benjamin D. Leibowicz

This project explores how physics-based and discrete-event simulation technologies can be jointly employed to model a suite of nuclear fuel fabrication facility designs with variable radiological environments, optimize their design to lower operational costs subject to a set of design constraints, and evaluate their performance. Initially, three variants of U-20Pu-10Zr metallic nuclear fuel in three specific geometric configurations are modeled and studied across more than 50 physics simulations in nuclear physics software packages SCALE and Monte Carlo N-Particle Transport (MCNP6.2). From these tests, values for effective dose rate and criticality are recorded for each of the nine alloy-geometry configurations.

These values are then incorporated into discrete-event models of fuel fabrication in the simulation program ExtendSim Pro 10 as process attributes. This allows one to track the dose to facility personnel as fuel is fabricated, dually enabling us to evaluate the safety

of a given facility design in terms of absorbed dose per worker per year and to craft operational guidelines that adhere to federal and local safety regulations.

Table of Contents

List of Tables

List of Figures

Chapter I: Introduction

The Versatile Test Reactor (VTR) program, announced by the Department of Energy (DoE) in 2017, aims to provide the United States state-of-the-art materials and advanced nuclear fuel testing capabilities in high neutron flux environments by 2026 [1]. Preliminary planning suggests that the VTR will be fueled by a metallic nuclear fuel (MNF), such as highly-assay low-enriched uranium (HALEU), plutonium-containing low enriched uranium (LEU+Pu), or plutonium-containing depleted uranium (DU-Pu). Since metallic nuclear fuels (MNF) have not been widely produced in the United States since the 1980s, and therefore a new source of metallic nuclear fuel must be created [2]. As part of its bid to operate the VTR, Idaho National Laboratory (INL) has expressed interest in manufacturing the fuel "in-house", leveraging its existing infrastructure and past experience handling such materials. While such a facility does not currently exist at INL, existing structures, such as the Fuel Manufacturing Facility (FMF) and Zero Power Physics Reactor (ZPPR) building, may be capable of housing such a complex, and thus facility designers have turned towards basing their designs around these buildings [3].

The fabrication of MNF is not a novel process being explored by the VTR program. Similar production facilities were built and operated by Argonne National Laboratory (ANL) throughout the latter half of the twentieth century during the operation of the Experimental Breeder Reactor II (EBR-II) [4]. However, the scale of the VTR program greatly surpasses its predecessor; where EBR-II produced only 62.5 MWt of power, the VTR is expected to produce anywhere between 110-130 MWt [5]. As such, the quantity of fuel needed to adequately supply the VTR will exceed the production capability of existing fabrication facility designs. Additionally, federal and local safety guidelines have become more conservative since the 1980's, placing more strict limits on annual dose and

17

criticality levels workers may encounter [6]. Thus, new floorplans and operating procedures must be designed to accommodate both the higher production demand and stricter safety regulations.

Using this proposed scenario as a test-case, in which the VTR program uses the FMF and ZPPR at INL to house its fuel fabrication facility, this project aims to design and evaluate a regiment of possible facility designs and operational policies using discrete-event simulation. Using production goals stated from literature and radiological data derived in the course this project, 12 distinct feasible facility designs and operating policies will be crafted and iteratively modified to optimize for cost reduction, all of which conform to the following design constraints:

1) Alloy Selection: the fuel material employed in the fuel fabrication process must be either, U-10Zr, U-20Pu-10Zr with an ^{241}Am concentration of 300 ppm, or U-20Pu-10Zr with an ^{241}Am concentration of 6000 ppm [1].

2) Scheduling: production must follow either a 5 days/week, 8 hours/day work schedule (5-8), or a 4 days/week, 10 hours/day work schedule (4-10).

3) Annual Fuel Assembly Throughput: the annual fuel assembly throughput of the fabrication facility must be sufficiently high such that a 40 fuel assembly per year production goal is met with 95% confidence, *P(throughput - 2σ ≥ 40) = 0.95* [3].

4) Criticality Limit: at no point in the fabrication process may the criticality of a glove box exceed 0.9. Systems which exceed this value could potentially put workers at risk of injury or death. Designs which fail to satisfy this goal cannot be considered feasible.

5)   Effective Dose Limit: the average worker handling fuel materials may not receive more than 2,000 mrem/y of effective dose. Facility layouts or hiring practices must be adjusted to ensure this limit is not exceeded.

6)   Glove Box Consolidation: the maximum number of fuel fabrication activities allowed per glove box will either be restricted to one or three.

7)   Facility Footprint: the total spatial footprint of any facility design must be less than 2,353 ft^2. Failing to adhere to this limit would suggest that fuel fabrication activities could not fit entirely within the FMF at INL, and would thus require the expansion existing buildings or the construction of entirely new structures.

Creating facility designs which satisfy the constraints listed above is accomplished by first modeling several fuel candidates in several geometric forms in two physics simulation software packages to derive radiation source terms, criticality values, and dose rate values. Then, several models of possible fuel fabrication facility designs will be modeled, iteratively optimized for cost reduction, and run in a discrete-event simulation program to generate worker dose, material demand, infrastructure demand, and project cost estimates.

Chapter II will provide the reader with background information regarding the technologies, concepts, and methodologies central to this thesis' work via a literature review. Chapter III will then detail the methods and techniques employed to characterize the above-mentioned radiological properties for a suite of fuel alloys in various geometric forms. After discussing the results gathered from this first set of simulations, Chapter IV will then detail the manner in which these results were integrated into 12 discrete-event simulation models and examine how said discrete-event models were constructed and optimized using discrete-event simulation. Finally, Chapter V, the conclusion of this

thesis, will embody a set of cost estimates, facility configurations, and operational guidelines that can be used to evaluate the merits of said designs. Ultimately, this thesis is not focused on designing the specific VTR fuel fabrication facility or hiring practices that the VTR program should consider; it is rather a demonstration of how nuclear simulation tools and operations research discrete event simulation software can be used together to evaluate the financial implications of various design and staffing considerations to produce the required number of fuel assemblies, with a high level of confidence, without exceeding nuclear safety constraints.

Chapter II: Literature Review

METALLIC NUCLEAR FUEL

MNF are a class of nuclear fuel characterized by their metallic composition. Unlike other commonly employed nuclear fuel types, such as oxides, dispersion, and particle fuels, all of which are variants on ceramics technologies, MNF are formed from either pure metallic elements or blended alloys [7]. Compared to their ceramic counterparts, MNF exhibit high levels of thermal conductivity, low heat capacity, and high degrees of ductility. These characteristics result in MNF being more resilient to failure in the face of abnormal reactor core operations. As such, MNF have been the leading candidate fuel-types for a variety of fast-spectrum reactor applications [8].

The fabrication of MNF is not a novel process being explored by the VTR program; similar production facilities were built and operated by commercial entities and Argonne National Laboratory (ANL) during the operation of the Experimental Breeder Reactor II (EBR-II) [9] throughout the latter half of the twentieth century. Fabricating MNF can be achieved in a number of manners, ranging from a plethora of molding techniques to atomization methods [10][11]. However, the technique explored by this study is the method originally employed at ANL to produce fuel for the EBR-II: injection casting [12]. In this process, ingots of fuel material (notably uranium and plutonium) and other non-fuel metals are first combined in a crucible and then melted in a casting furnace. After heating, the liquid metal is forced into fuel pin molds via an evacuation process, and upon cooling, said molds are removed to unveil a cast pin of alloyed metal. Following this, cast pins undergo several inspection steps to confirm that their dimensions, weight, and structure conform to fuel specifications. This process is relatively simple compared to other means

of producing nuclear fuel, and through years of successful employment, has become a proven and reliable practice [13].

In the scope of this thesis, three variants of U-20Pu-10Zr fuel, inhabiting four distinct geometries (approximating the form of fuel in the fuel assembly fabrication process), will be modeled in physics-simulation software to characterize their radiologic properties at various stages in the fuel fabrication process to ensure their designs and utilization conform to criticality and dose rate limits, all without hindering the fuel fabrication system's ability to meet fuel assembly throughput goals.

MONTE CARLO SIMULATION

Monte Carlo simulations, the namesake of the Monte Carlo N-Particle Transport Code System [14] (MCNP6.2) employed in this thesis, is an application of Monte Carlo methods that leverages the law of large numbers [15] and central limit theorem to derive numerical results for deterministic problems via the study of numerous independent, randomly sampled, simulated events [16]. Monte Carlo simulation techniques are employed in many fields of study, ranging from fluid dynamics to population growth, and are useful for modeling systems which are sufficiently large and/or complex as to make finding analytical solutions prohibitively difficult [17].

In the context of nuclear and radiation engineering, Monte Carlo simulation is frequently used to solve radiation transport problems, which is the study of how radiation (e.g. neutron radiation, photon radiation, etc.) interacts with and moves throughout its environment [18]. Radiation transport problems can be solved analytically. However, this is often a non-trivial process and is rarely employed lest the problem be sufficiently simplistic [19]; the effort to solve evenly moderately complex problems typically requires copious effort. Conversely, Monte Carlo simulations can be employed to describe highly

complex environment, as they provide answers to transport problems not by solving analytical solutions, but rather through generating a probabilistic description of the radiological environment in question [20]. In this practice, a pseudorandom number generator is employed to both assign the initial conditions of a particle's travel (i.e. its energy, direction, and origin) and determine the kinds of interactions the particle will undergo as it travels. The model tracks the particle from its birth until its death (the moment it is removed from the system), at which point the simulation begins the process again with a new particle. While running these tests may be computationally expensive (moderately complex problems typically require several millions of particle histories to be run in order to be adequately studied), the aggregated findings from each individual particle will approximate the true radiological behavior of the system with a high degree of accuracy, albeit with some small degree of stochastic error [18].

EFFECTIVE DOSE

Effective dose, E, is the "weighted equivalent doses in all tissues and organs of the body" [21]. While commonly determined with Monte Carlo codes solving fixed-source, steady state radiation transport problems (Eq. 2.1), effective dose may also be calculated with the use of Eq. 2.2, effective dose differs from absorbed dose, D, in that effective dose not only scales the impact of radiation in matter (i.e. the effective amount of energy imparted) based on both the type and energy of incident radiation, but also by the type of organ or tissue being irradiated, as not all tissues and organs are equally subject to the effects of irradiation [22]. Accurate estimating and reporting of one's effective dose is of the utmost importance in nuclear engineering, as it is one of the key metrics by which radiation workers are evaluated in determining if they have reached their federally-mandated 5 rem annual dose limit [23].

$$\bar{\Omega} \cdot \bar{\nabla}\psi + \Sigma_t \psi = Q + \int_0^\infty \int_{4\pi} \Sigma_s \psi d\Omega' dE' + \frac{\chi}{4\pi} \int_0^\infty \nu\Sigma_f \int_{4\pi} \psi d\Omega' dE' \qquad \text{Eq. 2.1}$$

$$E = \sum_T w_T H_T \qquad \text{Eq. 2.2}$$

CRITICALITY

Criticality, or more formally, the effective neutron multiplication factor, k_{eff}, is a non-dimensional parameter that characterizes the ability of a finite system to support self-sustaining fission [24]. Defined as the ratio of neutron production to neutron loss, the value of a system's k_{eff} can be interpreted to assign a system one of three classifications.

For $k_{eff} < 1$, a system is deemed "subcritical"; more neutrons are lost per neutron generation than are produced. Therefore, steady-state fission cannot be sustained. A system is designated "critical" when $k_{eff} = 1$. In this state, a steady-state fission chain can be maintained without the need for an external neutron source. Lastly, for values $k_{eff} > 1$, a system becomes "supercritical". In these states, the neutron population begins to exponentially increase, leading, in turn, to an exponential increase in fission events.

While often determined via the six-factor formula (Eq. 2.3), which defines the criticality of a system in terms of six of its physical properties, k_{eff} can also be determined via Monte Carlo codes solving the eigenvalue form of the Boltzmann transport equation (Eq. 2.4) [25]. Accurately estimating the criticality of a system (i.e. ensuring a system is safely below a specified criticality limit) is of paramount importance when designing nuclear facilities, as failing to do so can result in employee injuries and, in extreme circumstances, fatalities [26].

24

$$k_{eff} = \epsilon p \eta f P_{fnl} P_{tnl} \qquad \text{Eq. 2.3}$$

$$\overline{\Omega} \cdot \overline{\nabla} \psi + \Sigma_t \psi = Q + \int_0^\infty \int_{4\pi} \Sigma_s \psi d\Omega' dE' + \frac{1}{k} \frac{\chi}{4\pi} \int_0^\infty v\Sigma_f \int_{4\pi} \psi d\Omega' dE' \qquad \text{Eq. 2.4}$$

DISCRETE-EVENT SIMULATION

Discrete-event simulation (DES) is a form of systems modeling in which "items" (or other forms of traffic) flow through user-defined processes ("activities") along "connecters" in discrete time steps [27]. DES is employed in a number of disciplines, from systems manufacturing [28] to healthcare administration [29], and is a popular tool for studying the underlying intricacies and interactions within a system as well as its possible outcomes. Being stochastic in nature, DES also has the benefit of allowing one the ability observe a multitude of simulations with a single set of inputs; since events unfold via a series of probabilistic occurrences, a single model can produce a variety of outcomes. While other optimization methods exist, such as linear programming optimization and robust optimization [30], they rely on systems either being fully described by analytical equations or require all/most system uncertainties be given explicit, finite values, and are therefore relatively poor fits for this class and scale of problem. As such, not only are DES models useful tools for deriving stochastic results from highly complex systems, but their results can be leveraged to make informed decisions in the manufacturing context [31].

At its core, a discrete-event model is comprised of five key components [32]:

- Items: individual entities which flow through the system. Items can be unique or fungible, and can have "attributes" (local variables) assigned to them which can be used to achieve a number of effects, ranging from designating the item for specific tasks, to tracking their priority in a process, to logging item-specific information.

- Events: external occurrences which alter the state of the system.

- Activities: actions performed on items. Activities can involve one or multiple items and/or item types and have durations described by a probabilistic distribution (e.g. normal, exponential, triangular, etc.). Additionally, activities can be subjected to failures and shutdowns, also prescribed by a user-defined distribution.

- Resources: entities of limited quantity that activities compete for in order to operate. Common examples of resources include labor, tools, and components for manufacturing.

- Connectors: a visual representation of how materials, resources, and information flow throughout the system.

In the context of this thesis, DES is employed not only to design and optimize feasible MNF fabrication facility designs but to also derive cost estimates for said designs based on materials, infrastructure, and personnel demands.

Chapter III: Physics Simulations

Two metallic nuclear fuels have been proposed as candidates to fuel the Versatile Test Reactor (VTR) [1]:

1)   70 wt% low-enriched uranium, 20 wt% weapons-grade plutonium, and 10 wt% elemental zirconium (U-20Pu-10Zr)

2)   90 wt% low-enriched uranium and 10 wt% elemental zirconium (U-10Zr)

While U-20Pu-10Zr and U-10Zr fuels are proven technologies and have been manufactured in the United States in the past, the radiological profiles of these fuels are poorly characterized, especially in the context of the fabrication process. Since nuclear and radiation safety is of the utmost importance when handling radioactive material, understanding how these materials behave must be the first step in the facility design process.

In this thesis, the ORIGEN [33] and MCNP6.2 nuclear analysis software packages are used to simulate the radioactive decay and resulting neutral particle transport of various nuclear fuels in a representative glovebox environment. From these models, the effective dose rates, $\dot{E}$, to workers handling these fuels at various stages in the fabrication process and fuel criticality values can be determined. Finding the value of these limiting factors is the first task in an operational efficiency research project to demonstrate the ability to quantify the labor costs and facility requirements for fuel fabrication. The data collected from these software simulations will be compiled and imported into ExtendSim Pro 10 [34], a discrete-event simulation software being used in this thesis to plan and model the hypothetical VTR fuel fabrication facility. The results and models produced from this project could then be used to assist VTR facility designers in validating that designs and policies adhere to operational constraints and radiation dose and criticality limits.

METHODOLOGY

To calculate the effective dose rates generated by the UPuZr fuel in various geometries and isotopic compositions, one must first establish the intrinsic source terms associated with the unirradiated fuel. This is accomplished by modeling the decay of the fuel with respect to its isotopic composition and corresponding atomic density in ORIGEN.

A unique decay model is constructed and run for each of the representative fuel compositions listed in Table 3.1. Since the potential fuel feedstock has a wide range of compositions and the age of the Pu-241 defines the Am concentration via beta decay, three representative compositions were identified to simulate:

1)   Weapons-grade Pu in a U-20Pu-10Zr fuel with a low (0.03%) Am content (UPuAmZr-0.03)

2)   Weapons-grade Pu in a U-20Pu-10Zr fuel with a high (0.6%) Am content (UPuAmZr-0.6)

3)   U-10Zr (UZr)

In each ORIGEN simulation, the fuel alloy decays for a year in an unirradiated environment, with neutron and photon particle intensity metrics being recorded at the times listed in Table 3.2. Because there will be a time-delay from production of the fuel feedstock billets and fabrication of the fuel rods, these time periods account for a range of radiation decay and daughter product buildup after production. Additionally, by modeling the alloys over this timeframe, an intensity-time relationship can be derived for an alloy's neutron and photon radiation source terms while the fuel is being fabricated.

| | | Alloy | |
Nuclide	UPuAmZr-0.6	UPuAmZr-0.03	UZr
^{234}U	0.0002	0.0002	0.0003
^{235}U	0.0350	0.0350	0.0450
^{236}U	0.0002	0.0002	0.0002
^{238}U	0.6646	0.6646	0.8545
^{239}Pu	0.1800	0.1857	0.0000
^{240}Pu	0.0140	0.0140	0.0000
Zr	0.1000	0.1000	0.1000
^{241}Am	0.0060	0.0003	0.0000

Table 3.1:   Fuel isotopic composition. All values represent initial isotopic composition for each alloy in wt%. [1][35]

Sample	Sample Time (d)
1	0
2	1
3	5
4	7
5	14
6	30
7	180
8	365

Table 3.2:   Sample times in SCALE simulations.

Running each alloy through ORIGEN creates the source term neutron and gamma radiation profiles. The neutrons and photons in each model are binned according to energy, and each energy bin is assigned an intensity value representing the fraction of all particles contained within the energy bin. This creates discrete energy distributions for the neutron and photons for each alloy composition, which are later used in MCNP6.2 to define the source.

Throughout the course of the fabrication process, the fuel alloy will adopt four basic geometric forms:

1) Lumped Cube (LC): a cube of the raw alloy (Figure 3.1)

2) Cast Pin Array (CPA): 61 soda lime glass encased pins arranged in a hexagonal array with a pitch of 1 cm (Figure 3.2)

3) Finished Pin Array (FPA): 61finished pins (i.e. cylindrical fuel pins encased in type 304 stainless steel cladding and metallic sodium) arranged in a hexagonal array with a 1 cm pitch (Figure 3.3)

4) Fuel Assembly (FA): 434 finished pins arranged into two 217-unit hexagonal arrays (each with a pitch of 1 cm) stacked vertically on top of each another (Figures 3.3 - 3.5)

These forms are not strict recreation of the actual fuel form-factors one would expect to observe in practice; rather, these are representative forms that approximate the geometries are expected to assume during the fuel assembly fabrication process.
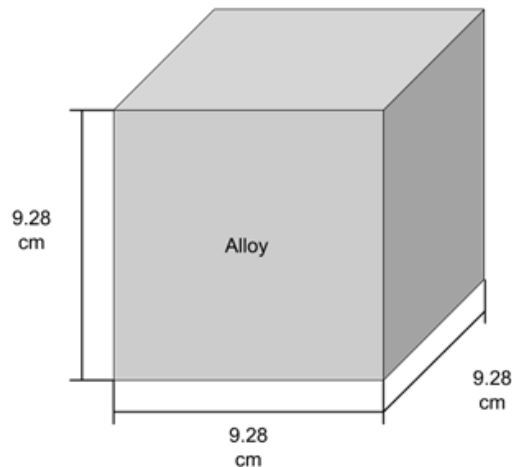
Figure 3.1:   Lumped cube geometric configuration.
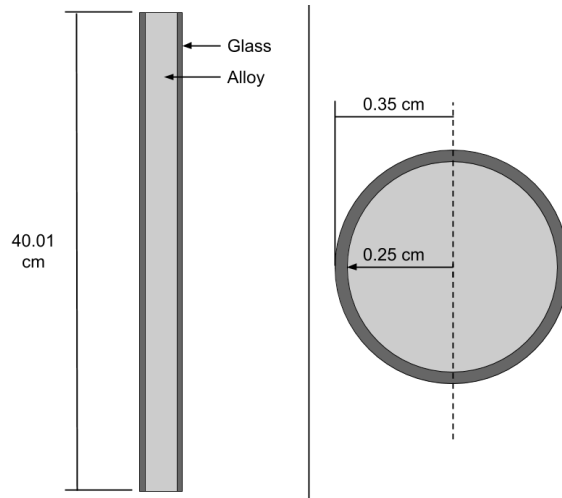
Figure 3.2:   Cast pin geometric configuration, viewed laterally (left) and from above (right). In MCNP6.2 models, 61 of these pins are arranged in a hexagonal array with a pitch of 1 cm.
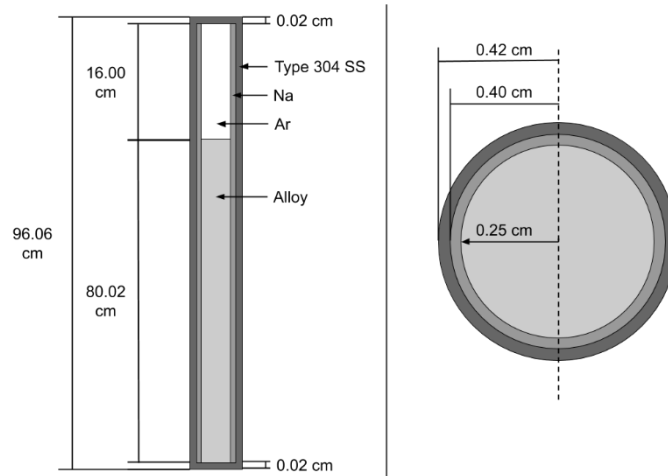
Figure 3.3:   Finished pin geometric configuration, viewed laterally (left) and from above (right). In MCNP6.2 models, 61 of these pins are arranged in a hexagonal array with a pitch of 1 cm.
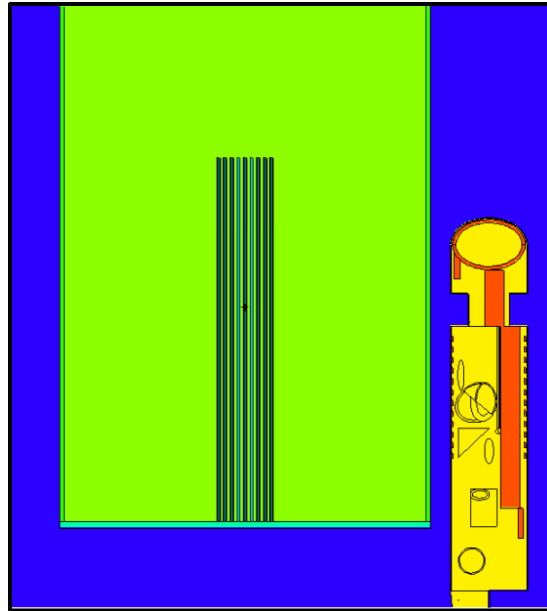
Figure 3.4:   Illustration of finished fuel assembly using MCNPX Visual Editor [36].
Assembly is pictured from the side.
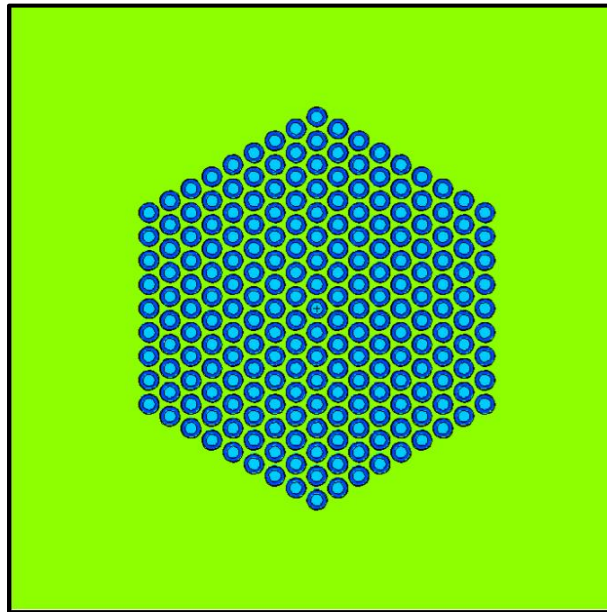
Figure 3.5:   Illustration of finished fuel assembly using MCNPX Visual Editor.
Assembly is pictured from above.

In addition to the three basic geometric configurations illustrated above, six additional geometric arrangements are modeled to explore how dose rates and criticality respond to consolidated glove box operations (i.e. multiple steps of the fabrication process occurring in a single glove box). These are represented via:

1) One lumped cube and one cast pin array per glove box (LC - CPA)

2) Two cast pin arrays per glove box (2 CPA)

3) One finished pin array and one cast pin array per glove box (CPA - FPA)

4) Two finished pin arrays per glove box (2 FPA)

5) Two fuel assemblies per glove box (2 FA)

6) Three fuel assemblies per glove box (3 FA)

Illustrations of the each of the above-listed configurations can be found in Appendix A. Allowing multiple processes to occur in a single glove box reduces the overall number of glove boxes needed for fuel fabrication activities, dually lowering infrastructure investments (and therefore total project costs) and reducing the overall footprint of said fuel fabrication facility design.

For each alloy-geometry configuration, three MCNP6.2 input decks are run to generate three sets of data: neutron effective dose rate, photon effective dose rate, and reactivity estimates.

Across each of these test scenarios, the geometry of the working environment is largely the same; a MIRD-ORNL-Male voxel phantom [37] stands at the center of a 7.42 x 2.49 x 4.38 m (width, depth, and height, respectively) [3] room whose ceiling and floor are modeled as 10.16 cm thick concrete. These dimensions approximate the environment at the FMF at INL (a potential location for MNF fabrication activities) and represent a glove box laterally surrounded by a 1.5 ft buffer. All exterior planes (including those above and below the concrete ceiling and floor) are modeled as reflective boundaries to simulate

33

an infinite array of glove boxes, all of which contain identical quantities of nuclear material. The phantom, standing 6 in away from the glove box, is modeled with arms reaching into an argon-filled glove box via two glove holes equipped with 1.5 cm-thick butyl gloves to simulate a worker handling the nuclear fuel.

The glove box has dimensions of 78 x 38 x 84 in and is raised 37.25 in off the ground by eight steel legs, with steel and leaded glass sides with dimensions listed in Table 3.3 [3][38]. Lastly, while the geometry of the fuel varies depending on its configuration (Figures 3.1-3.4), the fuel is always positioned in the center of the glove box, resting on the base plate of the glove box.

Side	Material	Thickness (cm)
Front	Leaded Glass	1.27000
Back	Leaded Glass	1.27000
Top	Type 304 SS	0.47625
Bottom	Type 304 SS	1.90500
Left	Type 304 SS	0.47625
Right	Type 304 SS	0.47625

Table 3.3:   Glove box component dimensions.

MCNP6.2 testing occurs in three phases: criticality simulations, neutron effective dose rate simulations, and then photon effective dose rate simulations.

The parameters governing these tests are identical across all alloy-geometry models (barring source particle intensities and energy distributions).

For criticality simulations, 200 total cycles, with 170 active cycles, of 50,000 source histories each cycle are simulated to estimate the reactivity of the system. These cycle and history counts were chosen to ensure all criticality estimates embodied standard deviations less than 0.001. Regardless of geometric configuration, the MCNP6.2 source definition

treats all fuel-containing cells as neutron sources and is equally likely to both sample any fuel-containing cell out of all total fuel cells and sample any point within each fuel containing cell as a source point.

For both neutron and photon effective dose rate tests, the energy distribution of source particles is specified on the SDEF to match the energy spectrum of 180-day old fuel alloy from the ORIGEN simulation. This alloy age is chosen because the neutron and photon profiles of the fuel alloys have reached relative equilibrium, which represents a reasonable maximum source-term. For the dose simulations, like the criticality source, the source definition treats all fuel-containing cells as neutron or gamma sources and is equally likely to both sample any fuel containing cell out of all total fuel cells and sample any point within each fuel containing cell as a source point.

F4 tallies are used to determine the average cell flux across an energy spectrum for different cells of the voxel phantom. The number of particle histories run for dose rate calculations are 20 and 500 million for neutron and photon dose rate tests, respectively. These values are sufficiently large to keep overall tally errors below 5%. Errors above 5% are generally considered unreliable, invalidating all but the highest-level findings derived with such data [14]. Additionally, low-error (i.e. approximately 1% error) findings were required in this stage to ensure the effects of dose rate and criticality uncertainty did not noticeably affect results gathered in the DES portion of this thesis, which itself has a stochastic uncertainty due to the failure of machinery.

Following the MCNP6.2 simulations, the collected F4 tally data for both neutron and photon tests are grouped according to alloy-geometry configuration, and the combined neutron-photon effective dose rate is calculated using Eq. 3.1, in which i, j, and k define all particle types, energies, and materials, respectively, and ϕ, $\mathfrak{R}$, and N represent the particle flux, response function, and particle source strength.

35

$$\left(\sum_{i}^{n,ph} \left(\sum_{j}^{energy \, (MeV)} \left(\sum_{k}^{material \, type} \phi_{i,j,k} \frac{1}{cm^2} \right) \cdot \Re_j(E) \frac{mrem \cdot cm^2}{particle} \right) \right)$$
$$\cdot N_i \frac{particles}{s} \cdot 3,600 \frac{s}{hr} = \dot{E} \frac{mrem}{hr} \quad \text{Eq. 3.1}$$

This function utilizes the energy-dependent dose coefficients as listed in ICRP 119 (Tables B.I-II) [21] and attributes a specific quantity of dose based on particle type (neutron or photon) and energy.

For each energy bin extracted from the MCNP6.2 output, the flux is first multiplied by the appropriate dose coefficient and then every dose-weighted flux is summed together to produce a dose burden per-source particle.

When this value is multiplied by a source particle intensity, a particle type-dependent effective dose rate in units of mrem/hour can be derived for a given alloy-geometry configuration. To calculate the final effective dose rate, the neutron and photon dose rate findings are simply summed together.

FUEL FABRICATION OPERATIONAL PLANNING

Ultimately, the radiological behavior metrics generated during ORIGEN and MCNP6.2 testing will be imported into ExtendSim Pro 10 to plan and model prospective VTR fuel fabrication facility designs. These dose-rate values will serve as time value multipliers which, when applied to DES models of potential VTR fuel fabrication facility designs, serve as model outputs which can both validate that models satisfy design constraints and direct the development of operation policies and floorplans that adhere to safety requirements.

Criticality findings will help determine whether a spatial layout and working mass of nuclear material at a given process adhere to criticality safety guidelines. Meanwhile, dose rate findings inform the staffing requirements needed to conduct said process.

The total dose burden of a given task in the fabrication process dictates the minimum number of full-time workers needed to maintain year-long operation of said task without exposing any individual worker beyond their annual dose limit, which would be organizationally defined and certainly below the NRC limit for radiation workers (5 rem/y). This reduced effective dose limit is representative of annual dose limits that institutions, such as the DOE laboratories, integrate into their ALARA ("as low as reasonably achievable") practices [39]. For this manuscript, a 2 rem/y limit will serve as the effective dose limit.

RESULTS

Simulations in ORIGEN produced source terms for the fuel alloys listed in Table 3.1. As detailed in Tables C.1 and C.2, neutron intensity levels remain stable throughout the simulation, decreasing by a maximum of 0.01% over all alloy-geometry combinations. However, the discrepancy in neutron intensity values between the UZr alloy and the UPuAmZr-0.6 and UPuAmZr-0.03 alloys is significant. Alloys UPuAmZr-0.03 and UPuAmZr-0.6, due to their increased concentrations of relatively short-lived actinides (^{239}Pu, ^{240}Pu, and ^{241}Am) produce nearly identical neutron intensities with values of approximately 560 n/s and 56,900 n/s when in fuel pin and lumped cube geometries, respectively. Meanwhile, alloy UZr, which lacks any transuranic content, only produces neutron intensities of 0.507 n/s and 51.6 n/s when in those same geometric configurations.

For the photon intensity data, found in Tables C.3 and C.4, the significant quantity of Am in the UPuAmZr-0.6 produces a much higher intensity. Photon emission intensity

37

remains relatively stable over time for both alloys UPuAmZr-0.03 and UPuAmZr-0.6, decreasing by a maximum of 0.15% across all configurations. Alloy UPuAmZr-0.6 exhibits the most intense photon output, producing approximately 6.80×10^{10} γ/s and 6.91×10^{12} γ/s when in fuel pin and lumped cube forms, respectively. In these same configurations, alloy UPuAmZr-0.03 produces more than an order of magnitude less: 6.45×10^9 γ/s and 6.56×10^{11} γ/s, respectively.

Meanwhile, the UZr alloy displays a unique photon intensity-time profile. In both geometric configurations, the alloy exhibits a 39% increase in photon emission intensity over the first 180 days of decay, rising from 1.69×10^6 γ/s to 2.35×10^6 γ/s for the fuel pin geometry and 1.72×10^8 γ/s to 2.39×10^8 γ/s for the lumped cube geometry.

This is due to the buildup of short-lived daughter radionuclides that appear in the fuel over time as the uranium content within the UZr alloy decays. However, this behavior changes at times greater than 180 days, when the activity of the fuel plateaus and remains constant with time. While this same phenomenon also occurs in the UPuAmZr-0.03 and UPuAmZr-0.6 alloys, its effects are muted in their emission-time behaviors. The Pu and Am radionuclide content in the UPuAmZr-0.03 and UPuAmZr-0.6, though less prevalent in terms of atomic abundance (Table 3.1), are far more active than their uranium radionuclide counterparts (Table D.1). As such, while the decay of uranium in the UPuAmZr-0.03 and UPuAmZr-0.6 alloys does contribute to an increase in photon emission intensity, the scale of this increase is negligible when compared to the larger but more stable photon emission from decay of ^{239}Pu, ^{240}Pu, and ^{241}Am.

MCNP6.2 criticality estimations indicate that criticality limits will not be a limiting factor in the design of facility layouts. As detailed in Tables 3.4 & 3.5, below, average k_{eff} values across all alloy-geometry configurations range between 0.07466 and 0.36401. With a 99% confidence interval, these values are extended to $0.07452 \leq k_{eff} \leq 0.36425$.

Assuming facilities enforce a strict subcriticality limit of 0.9, even the most active, densely-arranged alloy-geometry configuration (i.e. UPuAmZr-0.6 in lumped cube form) will still embody a safety factor of over 2.4.

| Configuration | $k_{eff} \pm \sigma$ | | |
	UZr	UPuAmZr-0.03	UPuAmZr-0.6
LC	0.23696 ± 0.00007	0.36401 ± 0.00009	0.36023 ± 0.00010
CPA	0.07466 ± 0.00005	0.10893 ± 0.00006	0.10816 ± 0.00005
FPA	0.16104 ± 0.00010	0.22335 ± 0.00010	0.22105 ± 0.00010

Table 3.4:   Criticality values for basic alloy-geometry configurations.

| Configuration | $k_{eff} \pm \sigma$ | |
	UZr	UPuAmZr-0.03
LC – CPA	0.23704 ± 0.00008	0.36379 ± 0.00012
2 CPA	0.08341 ± 0.00006	0.11755 ± 0.00007
CPA - FPA	0.15545 ± 0.00010	0.21845 ± 0.00010
2 FPA	0.19316 ± 0.00011	0.25635 ± 0.00014
3 FPA	0.22923 ± 0.00014	0.29277 ± 0.00013

Table 3.5:   Criticality values for consolidated glove box configurations.

An additional, accident-case scenario, in which a lumped cube of UPuAmZr-0.03 (the most critical configuration) was placed in a glove box filled with room-temperature water, was modeled and run in MCNP6.2 to study its effect on criticality. The water, acting as a moderator and reflector, did result in an increase in k_{eff}, raising criticality from 0.36401 to 0.56559. However, this value is still far below the assumed 0.9 criticality limit.

These findings suggest that, at any stage in the fuel fabrication process, either the current material mass limits can be substantially increased or the spacing between glove boxes can be substantially decreased without fear of exceeding subcriticality limits. However, in adjusting one or both of these parameters, a higher dose rate will be incurred

and the reactivity of the system will increase. Auxiliary MCNP6.2 tests reveal that both dose rate and criticality exhibit a negligible decrease as glove boxes become increasingly spaced apart. Conversely, the degree to which dose rate and criticality increase to increases in the quantity of fuel mass per glove box can be observed in Table 3.5 and Figure 3.7.

As detailed in Tables E.7-E.16, estimated effective dose rates are dominated by the photon-based ionizing radiation and are highly dependent on the isotopic composition and geometric configuration of the fuel. This volatility results in calculated effective dose rates with values that span three orders of magnitude, ranging from a minimum of $0.0273 \pm 1.49 \times 10^{-4}$ mrem/h to a maximum of 55.4 ± 0.073 mrem/h.

As illustrated in Fig. 6, the smallest of these effective dose rates are exhibited by fuels crafted from UZr alloys. As the fuel alloy is changed to include higher concentrations of transuranic content, the effective dose rate progressively grows. By replacing UZr with UPuAmZr-0.03 or UpuAmZr-0.6 alloys, the effective dose rate increases by an average of 3,226% and 30,696%, respectively. A distinct trend can be observed in terms of the fuel's geometry as well. As detailed in Table 3.6, across all alloys, dose rates are minimized when in the lumped cube configuration and are maximized when in fuel assembly configuration. On average, changing the geometry of the fuel from a lumped cube form to a finished pin array will increase the effective dose rate by 53.3%. Relative to their lumped cube counterpart, the increase in dose rate for cast pin arrays and fuel assemblies are 86.0% and 558.9%, respectively.

| | Dose Rate (mrem/h) | | | |
Alloy \ Geometry	LC	CPA	FPA	FA
UZr	2.724×10^{-2}	6.074×10^{-2}	5.577×10^{-2}	2.380×10^{-1}
UPuAmZr-0.03	1.165×10^{0}	1.871×10^{0}	1.545×10^{0}	6.850×10^{0}
UPuAmZr-0.6	1.075×10^{1}	1.874×10^{1}	1.317×10^{1}	5.538×10^{1}

Table 3.6:   Dose rates for basic fuel-geometric configurations.
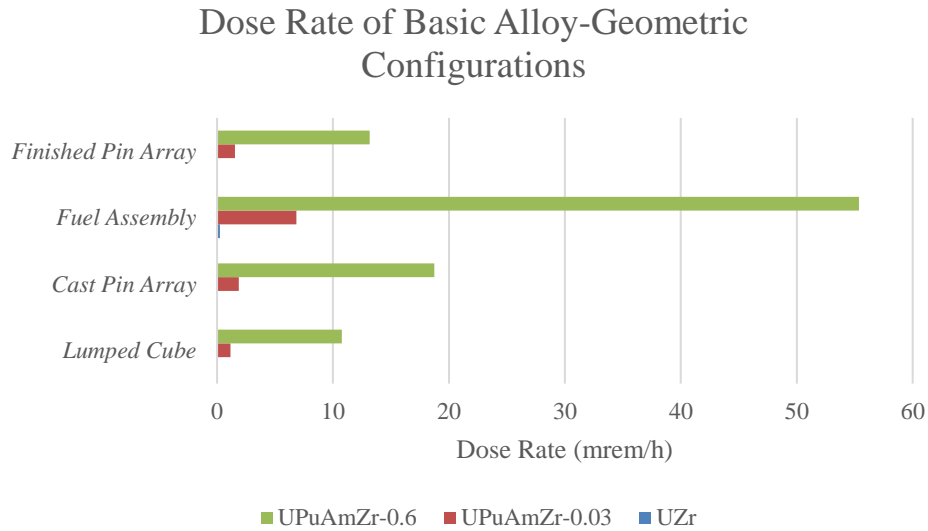
Figure 3.6:   Coupled bar graph of effective dose rates for all basic alloy-geometry configurations.

As detailed in Tables E.1-E.16, dose rates for fuels in consolidated glove box arrangements span values from $0.0481 \pm 3.17 \times 10^{-4}$ to $0.441 \pm 2.74 \times 10^{-3}$ for scenarios in which UZr fuel is employed and 1.23 ± 0.106 to 13.3 ± 0.189 for scenarios in which UPuAmZr-0.03 fuel is employed. These findings suggest that dose rate does not respond to consolidation in a purely additive manner; the total estimated dose rates from a given configuration are less than the sum of the dose rates from the individual fuel geometries in the system.

This thesis does not explore test cases in which UPuAmZr-0.6 fuel is handled in a consolidated glove box environment, as the dose rates exhibited by UPuAmZr-0.6 fuels in basic geometric configurations were already alarmingly high, and would require untenable levels of redundancy hires to be made for said configurations to be viable. This effect would only be exaggerated in consolidated glove box arrangements, and thus was not explored as a possible test scenario.

Dose Rate of Consolidated Glove Box Configurations
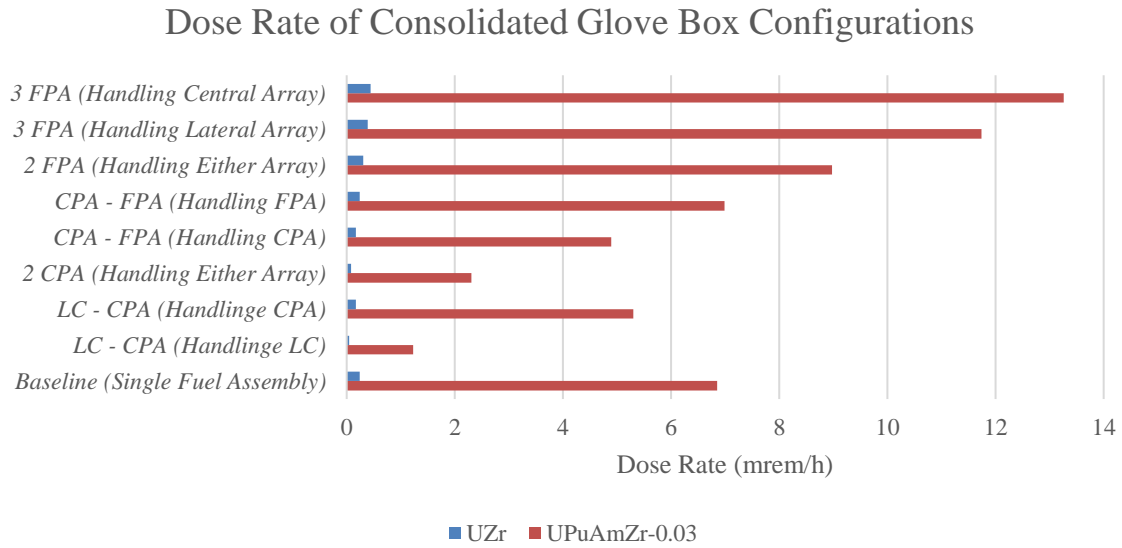
Figure 3.7:   Coupled bar graph of effective dose rate for consolidated glove box configurations.

Assuming each task in the fuel fabrication process requires full-time staffing to adequately support the VTR mission, personnel needs for each task will vary depending on the dose rate burden attributed to handling the appropriate fuel alloy-geometry configuration. Using the data in Tables E.7-E.16, staffing requirements can be formulated for each using Eq. 3.2.

$$S_j = \left\lceil \frac{2{,}000 \, \frac{mrem}{year}}{\dot{E}_j(alloy, geometry) \, \frac{rem}{worker-year}} \right\rceil \qquad \text{Eq. 3.2}$$

42

In dividing the assumed annual effective dose limit by the calculated effective dose rate for each fuel configuration, $\dot{E}_j$, and applying a ceiling function to this calculation, the minimum number of workers, S_j, needed to handle the fuel for a given process over a full working year (defined as 1,600 h per year) is determined.

As detailed in Tables 3.7 & 3.8, the utilization of the UZr alloy will demand the lightest personnel requirements, as each task in the fuel fabrication process requires, at most, a single, full-time worker, regardless of whether a consolidated glove box is employed or not. In either configuration, a single worker can perform their duties for a full work year while receiving a maximum of 705.3 mrem during that time. By comparison, if alloys UPuAmZr-0.03 or UPuAmZr-0.6 are to be employed, the most dose-intensive tasks will incur a dose burden of 10,959 and 88,601 mrem over the course of a single year, respectively. These dose rates greatly exceed the affixed 2 rem/y limit, and would thus require anywhere between 6 and 45 individuals to be hired to perform the same tasks to replace workers who reach their annual effective dose limits.

Alloy and Configuration, j		Annual $E_j \pm \varepsilon_j$ (mrem)	S_j
UZr	Lumped Cube	43.58 ± 0.307	1
	Cast Pin Array	97.27 ± 0.361	1
	Finished Pin Array	89.23 ± 0.343	1
	Fuel Assembly	380.7 ± 1.87	1
UPuAmZr-0.03	Lumped Cube	$1{,}864 \pm 27.2$	1
	Cast Pin Array	$2{,}993 \pm 24.8$	2
	Finished Pin Array	$2{,}471 \pm 26.9$	2
	Fuel Assembly	$10{,}959 \pm 116$	6
UPuAmZr-0.6	Lumped Cube	$17{,}200 \pm 113$	9
	Cast Pin Array	$29{,}981 \pm 136$	15
	Finished Pin Array	$21{,}069 \pm 106$	11
	Fuel Assembly	$88{,}601 \pm 116$	45

Table 3.7: Minimal staffing requirements, S_j, for safe, full-time operation when handling fuel in basic alloy-geometry configurations.

Alloy and Configuration, j		Annual $E_j \pm \varepsilon_j$ (mrem)	S_j
UZr	LC – CPA (Handling LC)	77.0 ± 0.51	1
	LC – CPA (Handling CPA)	270.1 ± 0.51	1
	2 CPA (Handling Either)	126.8 ± 0.58	1
	CPA – FPA (Handling CPA)	270.7 ± 1.67	1
	CPA – FPA (Handling FPA)	389.2 ± 1.67	1
	2 FPA (Handling Either)	116.4 ± 0.55	1
	2 FA (Handling Either)	487.6 ± 2.99	1
	3 FA (Handling Lateral Array)	624.7 ± 4.39	1
	3 FA (Handling Central Array)	705.3 ± 4.39	1
UPuAmZr-0.03	LC – CPA (Handling LC)	$1{,}964.6 \pm 169.4$	1
	LC – CPA (Handling CPA)	$8{,}480.96 \pm 169.4$	5
	2 CPA (Handling Either)	$3{,}688.6 \pm 42.0$	2
	CPA – FPA (Handling CPA)	$7{,}830.1 \pm 177.5$	4
	CPA – FPA (Handling FPA)	$11{,}181.4 \pm 177.5$	6
	2 FPA (Handling Either)	$2{,}949.1 \pm 35.7$	2
	2 FA (Handling Either)	$14{,}359.2 \pm 178.4$	8
	3 FA (Handling Lateral Array)	$18{,}785.6 \pm 301.7$	10
	3 FA (Handling Central Array)	$21{,}217.6 \pm 301.7$	11

Table 3.8:   Minimal staffing requirements, S_j, for safe, full-time operation when handling fuel in consolidated glove box configurations.

The results from the physics simulations provide great insight as to the radiological properties of the candidate fuels will impact fuel assembly production. Namely, not only has it been shown that criticality will not be a binding constraint for any designs being explored, but that fuel alloy selection greatly impacts expected employee dose rates, with UZr fuels incurring the smallest dose burden and UPuAmZr-0.6 fuels incurring the greatest. Additionally, the geometric form and arrangement of fuel-geometry units also impacts employee dose. Ultimately, the dose rate values listed in Tables 3.6 and 3.7 will be imported into DES models of potential fuel fabrication facility designs, as will be elaborated on in the next chapter.

Chapter IV: Discrete-Event Simulation

In order to support "in-house" production of MNF at INL, not only must a new fuel fabrication facility be crafted, but operational policies must also be established to ensure fuel production meets the demands of the VTR mission while also adhering to local and federal safety regulations. These baseline design constraints (summarized in Table 4.1) are inflexible and must be satisfied for a given set of facility designs and operational policies to be considered a feasible design candidate [40]. Conversely, failing to meet these demands suggests the design is either incapable of producing the required quantity of MNF, violates radiation safety regulations, or both, and thus cannot be employed.

Design Constraint	Value
Alloy Selection	UZr, UPuAmZr-0.03, or UPuAmZr-0.6
Scheduling	5 days/week, 8 hours/day
Criticality Limits	$k_{eff} \leq 0.9$
Effective Dose Limits	$E \leq 2{,}000$ mrem/year
Throughput Confidence	$P(throughput - 2\sigma \geq 40) = 0.95$
Glove Box Consolidation	Disallowed, Allowed
Facility Footprint	$\leq 2{,}353$ ft^2

Table 4.1:   Baseline DES design constraints [3].

In this thesis, DES software ExtendSim Pro 10 is employed to construct, optimize, and evaluate 12 potential INL MNF fabrication facility designs. Aside from a single model which adheres to the constraints listed above, each model explored represents a unique scenario in which the fabrication process is subject to different design constraint values. In running these models and collecting their fuel assembly production, dose rate, and construction data, not only will we be able the conclude how an optimal design of the MNF

fabrication facility responds to changes in operational demands, but also determine how design constraints drive project costs.

METHODOLOGY

The first step in creating our 12 scenario models is creating an initial, feasible DES model that can later be optimized and tailored to varying sets of design constrains. This is accomplished by first creating an unoptimized, infeasible model which incorporates the fundamental processes that define MNF fabrication and accurately represents the flow of materials between said processes.

The underlying structure of this basic model is based on existing facility designs which were once employed to fabricate MNF in support of the EBR-II [12]. This design, illustrated in Figure 8, describes the potential casting process to be employed for VTR fuel fabrication, but provides basic material input demands, processing times, and material flow information that is vital to constructing DES models which accurately reflect the MNF injection casting process.
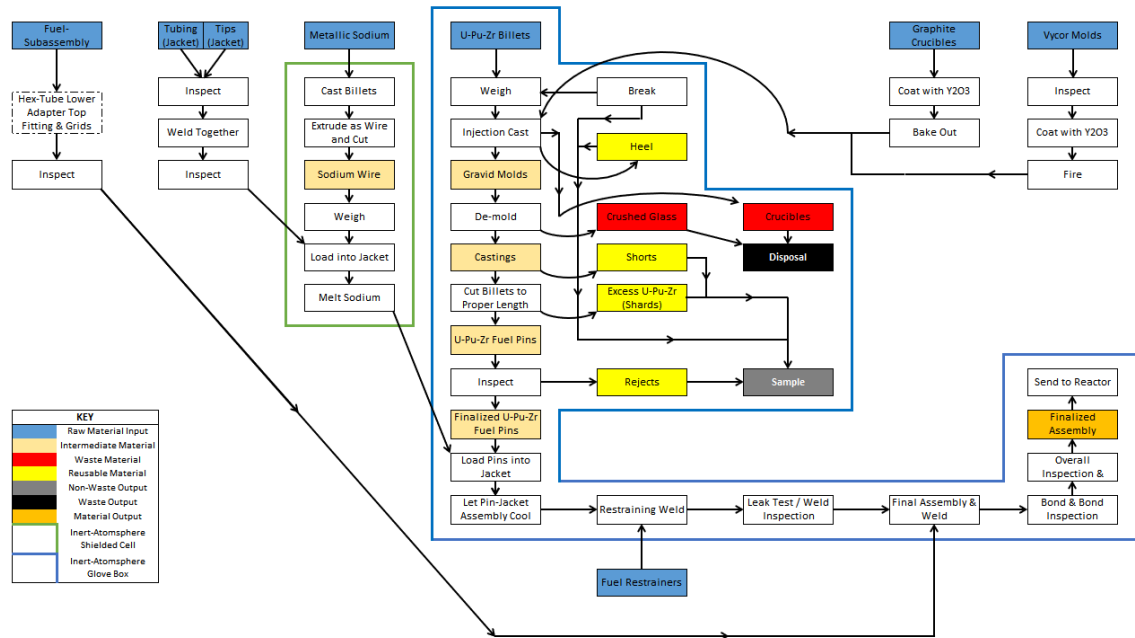
Figure 4.1:   High-level flowchart of the metallic nuclear fuel fabrication process [12].

The initial DES model is comprised of 6 subsystems, each roughly correlating to a production line following one of the material input streams illustrated in Figure 4.1. These subsystems are:

1) Pin Casting Subsystem: the subsystem in which fuel pins are cast, refined, inspected, and assembled into fuel assemblies. This is the only subsystem in which radioactive material is handled.

2) Crucible Subsystem: the subsystem where graphite crucibles and Vycor glass molds are prepared and bundled for injection casting.

3) Pin-Jacket Fabrication Subsystem: the production line in which type 304 stainless steel is bent, welded, and assembled into fuel-pin jackets.

4) Sodium Bonding Subsystem: the subsystem in which metallic sodium is cut, loaded into, and bonded with the type 304 SS jackets.

48

5) Subassembly Subsystem: the production line where subassembly hardware is received and prepared for bundling with finished fuel-pins.

6) Assembly Subsystem: the final subsystem where finished fuel-pins and subassembly hardware are combined and tested to form fuel assemblies.

In total, there are ten key steps in the fuel pin production process [41][12]:

1) Alloy preparation: the alloy is collected and weighed to ensure the appropriate amount of metal is being cast. In this step, a worker will also bundle the alloy with a graphite crucible and casting molds ahead of casting.

2) Casting: upon being loaded into a casting furnace, the alloy is melted in the crucible and, via an evacuation process, is vacuum cast into its molds.

3) Cast Pin Inspection: after cooling, the cast pins and leftover alloy heel are removed from the casting chamber. Each cast pin is examined to ensure that it is undamaged and fully formed. Pins which fail this inspection are discarded and recycled back into the casting process.

4) Pin Demolding/Heel Crushing: pins which pass inspection are removed from their glass molds. Said molds are then discarded as contaminated waste. Concurrently, the heel leftover from the casting process is crushed and recycled back into the casting process.

5) Pin Measurement: cast pins are examined to determine if they conform to length, width, mass, and surface porosity standards. Pins which pass this examination proceed through the fabrication process; those that fail are discarded and recycled into the alloy casting process.

6) Pin Cutting: cast pins are cut and ground to a specified length in preparation for being inserted into a fuel-pin jacket.

49

7) Fuel-Pin Jacket Welding: after being inserted into the sodium-bonded jacket, the jacket is welded shut to entirely sheath and contain the fuel pin. Upon completion, the fuel-pin jacket is inspected to ensure the jacket is satisfactorily welded and the sodium has bonded with the fuel alloy. Failing this inspection results in the fuel-pin jacket being de-welded and reassembled.

8) Fuel-Pin Jacket Bonding: pins nested in sodium-bound jackets are heated to bind the MNF alloy to the sodium.

9) Assembly Fabrication: finished fuel-pins are batched with subassembly hardware to form final fuel assemblies. Upon completion, the assembly is inspected to check for compliance with manufacturing tolerances. Failing said inspection results in the assembly being reassembled and retested.

10) Final Assembly Inspection: the finalized fuel assembly is subjected to a litany of tests to validate the integrity of its construction and assess the assemblies' thermal and radiological behavior. Assemblies that pass this inspection can be deployed or stored for future use. Assemblies which fail are deemed total losses and are discarded.

Translating the flowchart in Figure 8 and the steps listed above into a DES model in ExtendSim yields an initial, infeasible and unoptimized model (depicted in Figure 4.2). In this model, each "activity" block corresponds to a key process outlined by Walter, Golden, and Olson (1975). Inter-block connections reflect the flow of materials illustrated in Figure 4.2, and "queue" blocks and "batch/unbatch" blocks are positioned in areas in which employees must interact with fuel materials and/or steps in which material streams are combined.

50
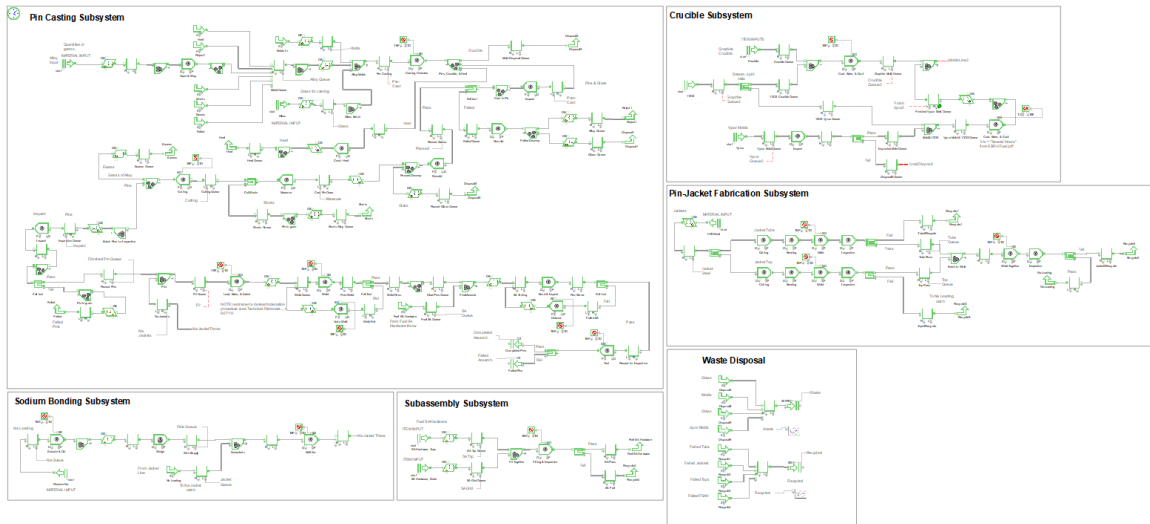
Figure 4.2:   Initial DES model of the MNF fabrication process as described by Walter, Golden, and Olson (1975).

Model Inputs

With the structure of the initial DES model established, input data must now be applied to the "activity", "batching", and "selection" blocks placed throughout the model. "Activity" blocks require two forms of input: process time distributions and failure rate distributions. The former of these categories describes the range of times an activity can take to complete as a random variable with a user-defined probability distribution. With the exception of Na wire extrusion, every task in the MNF fabrication process is modeled to exhibit a normal distribution in its process times. Average process times and standard deviation values for each task in the fabrication process are listed in Tables 4.2-4.4, and are derived from literature, when available [42][41]. For processes with unspecified mean times, reasonable approximations were assigned. Additionally, an assumed standard deviation equal to 3.16% the mean (a 10% variance) was applied to processes with standard deviations which have not been estimated in literature.

51

The second category of "activity" block inputs are failure rates. Unlike process time distributions, machine failure rates are described by exponential distributions with an assumed mean of 100,000 minutes. Data for this value, like the process standard deviation times mentioned above, is not readily available in the literature and thus has an assumed value which was implemented to allow the model to behave in a realistic manner (i.e. one in which processes are accomplished in a range of times and machines occasionally fail). If better process time and failure rate parameters are developed in the future, they can be supplemented into the model without compromising its integrity. Likewise, repair times are described by exponential distributions and embody a mean of 100 min. If a process fails midway through a task, the model simply keeps the items and restarts the process from the beginning upon being fixed. For tasks which are not reliant on machinery, no failure rate is prescribed.

Batching values, applied to "batch/unbatch" blocks, describe the types and counts of materials required to initiate a process which requires workers and/or the combination of multiple types of materials. Again, summarized in Tables 4.2-4.5, batch sizes are derived from literature [3][41][42].

Finally, "selection" blocks are used to simulate items passing/failing inspections. When stated in literature, specific tasks are given unique pass:fail ratios. Such tasks include post-demolding pin dimensioning and post-cutting pin inspections. However, for all other inspections, a generic 5% failure rate is assumed.

Task	Distribution	Mean, μ (min)	Std. Dev., σ (min)	Batch Size
Weigh Alloy	Normal	15	1.225	12,500 g
Load/Unload Furnace	Normal	15	1.225	1 batch
Casting	Normal	685	8.276	1 batch
Crush Heel	Normal	15	1.225	5,000 g
Inspect Cast Pins	Normal	60	2.449	61 cast pins
Demold Cast Pins	Normal	15	1.225	61 cast pins
Measure Cast Pins	Normal	60	2.449	61 cast pins
Cut Cast Pins	Normal	60	2.449	61 cast pins
Inspect Cut Pins	Normal	60	2.449	61 cast pins
Load/Unload Jackets	Normal	15	1.225	61 clad pins
Weld Jackets	Normal	120	3.464	61 clad pins
Un-weld Jackets	Normal	120	3.464	61 clad pins
Bond & Inspect	Normal	210	4.583	220 clad pins
De-bond	Normal	210	4.583	220 clad pins
Final Inspection	Normal	60	2.449	1 assembly

Table 4.2: Pin production parameters. Note: "1 batch" = 12,500 g of alloy, 1 graphite crucible, and 100 Vycor glass casting molds. "1 clad pin" = 1 cast pin and 1 Na-bonded jacket. "1 assembly" = 220 clad pins and 1 steel fuel sub-assembly.

Task	Distribution	Mean, μ (min)	Std. Dev., σ (min)	Batch Size
Cut Jacket Tubes	Normal	60	2.449	10 tubes
Bend Jacket Tubes	Normal	60	2.449	-
Weld Jacket Tubes	Normal	60	2.449	-
Inspect Jacket Tubes	Normal	60	2.449	-
Cut Jacket Tops	Normal	60	2.449	20 tops
Bend Jacket Tops	Normal	60	2.449	-
Weld Jacket Tops	Normal	60	2.449	-
Inspect Jacket Tops	Normal	60	2.449	-
Weld Jackets	Normal	60	2.449	10 tubes, 20 tops
Inspect Jackets	Normal	60	2.449	10 tubes, 20 tops

Table 4.3:   Jacket production parameters.

Task	Distribution	Mean, μ (min)	Std. Dev., σ (min)	Batch Size
Load & Coat Crucible	Normal	30	1.732	1 crucible, 100 g Y_2O_3
Bake Crucible	Normal	540	6.928	-
Unload Crucible	Normal	15	1.225	-
Inspect Vycor Glass	Normal	15	1.225	100 molds
Load & Coat Glass	Normal	30	1.732	100 molds, 100 g Y_2O_3
Bake Glass	Normal	300	5.477	-
Unload Glass	Normal	15	1.225	-

Table 4.4:   Molds (Vycor glass and crucible) production parameters.

Task	Distribution	Mean, μ (min)	Std. Dev., σ (min)	Batch Size
Extrude Na	Constant	0.0642	-	1 g Na
Weigh Na	Normal	15	1.225	300 g Na
Load Na & Jacket	Normal	15	1.225	16 jackets, 48 g Na
Bond Na & Jacket	Normal	480	6.928	-
Unload Na-bonded Jacket	Normal	15	1.225	-

Table 4.5:   Na-bonded jacket production parameters.

Optimization

Given the size and complexity of the DES model created, arriving at an optimal configuration via analytical techniques would be exceedingly difficult, if not impossible [43]. Instead, models of this nature must be examined both in terms of their real-time functions and post-facto outputs in order to identify how the system can be modified to move towards optimality [44]. While there is no guarantee this *ad hoc* approach will arrive at a true global optimum [45], progress can be made in optimizing the model to one's degree of satisfaction. As such, this thesis employs a manual, algorithmic approach to optimizing model the structure and operational policies for the MNF fabrication facilities to minimize the total equivalent system cost while simultaneously satisfying all of the design constraints which characterize the scenario (illustrated in Figure 4.3).
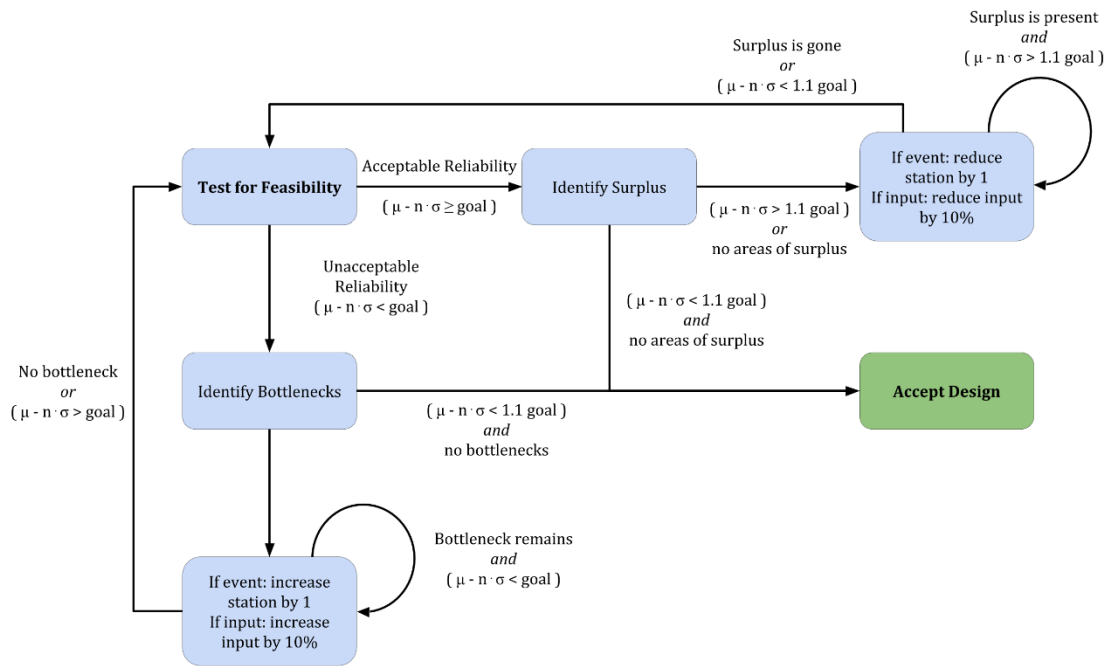
Figure 4.3:   Flowchart illustrating the optimization algorithm.
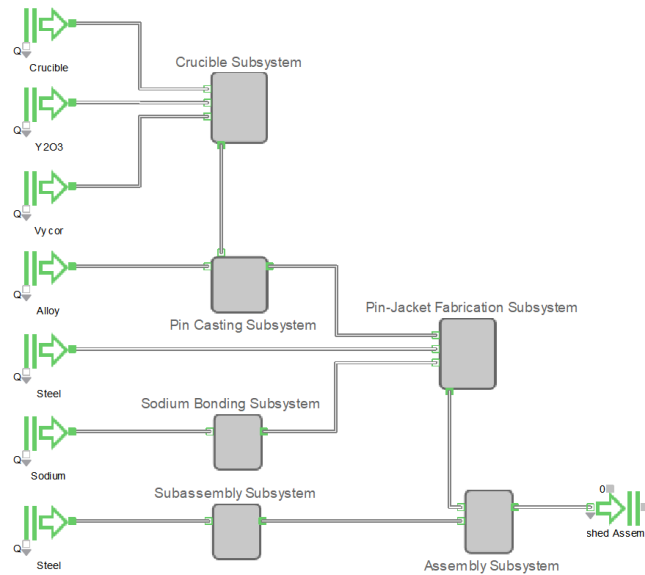
Figure 4.4:   Hierarchical model of the nuclear fuel fabrication process in ExtendSim Pro 10 illustrating the six major subsystems of this process and their relationships.

Starting with any DES model, the model is run 20 times, and at the end of each simulation results are recorded. Upon completion of these simulations, the average number of passed fuel assemblies over the 20 simulations is examined to see if the model is feasible (i.e. the assembly throughput constraint has been satisfied). Failing this test, the model's subsystems are examined for signs of bottlenecks (illustrated in Figure 4.4). This is accomplished by stepping backwards through the model (i.e. going from the last step to the beginning) and examining the charts of the subsystem queues along the way until the first signs of bottlenecking are spotted (see Figure 4.5). Once identified, the subsystem in question is explored by again examining the process queue charts in reverse order. Like with the subsystem charts, upon identifying a process exhibiting signs of bottlenecking, the model is modified by either:

- Duplicating the "activity" block if the process causing bottlenecking is a process.
- Increasing material input rate by 5% if the bottleneck is due to insufficient material resources.

Upon making this change, another set of 20 simulations are run. If said change results in the model becoming a feasible design, then the algorithm is restarted, this time checking for areas of surplus. Conversely, if the model remains infeasible, modification is repeated until either the bottleneck is relieved or duplicating the "activity" blocks/increasing the material input rates no longer yield improvements. In the former case, the entire algorithm is restarted; in the latter, the subsystem graph search is continued into the next subsystem exhibiting bottlenecking, and a new culprit "activity"/"input" block is identified and the modification process is repeated.
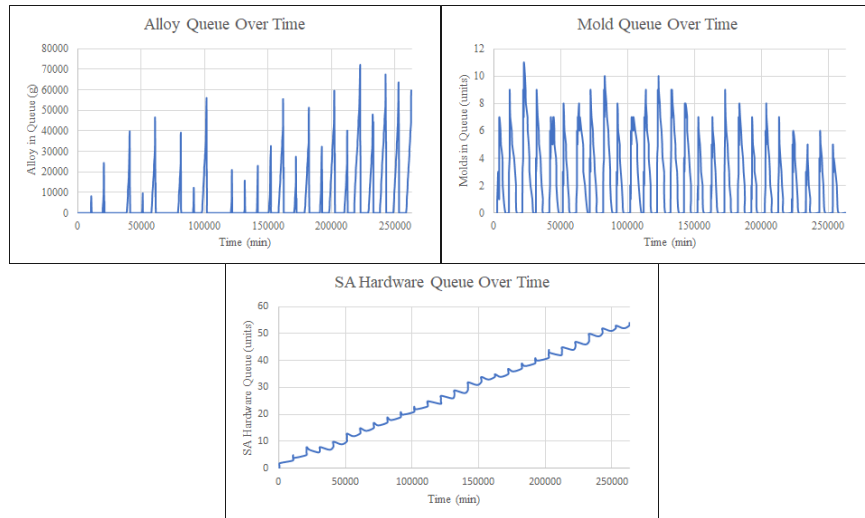
Figure 4.5:   Example subsystem graphs exhibiting signs of bottlenecking (top-left), optimality (top-right), and surplus (bottom).

In the case that the model is determined to be feasible after 20 simulations, the model is examined for inefficiency (i.e. areas of surplus). In a similar process as before, the queue graphs of the various subsystems are examined, albeit this time in sequential order. Upon recognizing the first instance of surplus accumulating, the culprit subsystem is probed in production-sequential order until a process graph exhibiting surplus behavior is identified. Like before, the model is modified in one of two ways:

- An "activity" block is removed if the surplus originates from a process.
- The material input rate on an "input" block is reduced by 5% if the surplus originates from overproduction of a resource item.

Upon making this change, the model is rerun for another 20 trials, and a feasibility check is performed. If the system is determined to be infeasible, the previous change is undone and the subsystem graph search is restarted to identify remaining areas of surplus. Conversely, if the modification fails to remedy the surplus, the process is repeated until

either the process reaches optimality (see Figure 4.5), or the repeated reductions fail to affect change. With either outcome, the entire algorithm is restarted.

While the rate of optimality convergence has yet to be characterized for this algorithm, this process has been successfully employed to produce satisfactorily optimized MNF fabrication facility designs. Following this algorithm, the first infeasible model (depicted in Figure 4.2) is iteratively redesigned until it achieves feasibility and assumes the forms depicted in Appendix F. From there, these models are further refined into 12 distinct models using the above-described optimization algorithm until they optimally satisfy the set of design constraints outlined in the next section.

Testing Scenarios

12 testing scenarios were selected for modeling to observe how changes to design constraint values impact project costs, optimal fabrication facility layouts, and overall facility performance. Some design constraints, such as fuel assembly throughput and criticality limits, remained unaltered between all of the testing scenarios, as they could not be increased or decreased without either fundamentally changing the scope of the optimization question or could not reasonably be applied to a real nuclear facility. However, other design constraints, such as alloy selection, work schedules, dose limits, production confidence, and the consolidation (or lack thereof) of glove box operations could be altered without undermining the validity of the test case. Of the 12 cases presented in Table 4.6, Scenario 2 will be considered our baseline scenario, as it most closely adheres to the operating policies most likely to be employed by the VTR program [3].

	Scenario #	Alloy	Hrs/Day	Dose Limit	Confidence	Consolid.?
Alloy Selection	1	UZr	8	2 rem/y	$\mu - 2\sigma \geq 40$	No
	2	UPuAmZr-0.03	8	2 rem/y	$\mu - 2\sigma \geq 40$	No
	3	UPuAmZr-0.6	8	2 rem/y	$\mu - 2\sigma \geq 40$	No
4-10 Schedule	4	UZr	10	2 rem/y	$\mu - 2\sigma \geq 40$	No
	5	UPuAmZr-0.03	10	2 rem/y	$\mu - 2\sigma \geq 40$	No
	6	UPuAmZr-0.6	10	2 rem/y	$\mu - 2\sigma \geq 40$	No
Strict Dose Limit	7	UPuAmZr-0.03	8	0.5 rem/y	$\mu - 2\sigma \geq 40$	No
	8	UPuAmZr-0.03	10	0.5 rem/y	$\mu - 2\sigma \geq 40$	No
Lowered Confidence	9	UPuAmZr-0.03	8	2 rem/y	$\mu - \sigma \geq 40$	No
	10	UPuAmZr-0.03	10	2 rem/y	$\mu - \sigma \geq 40$	No
Condensed Operation	11	UPuAmZr-0.03	8	2 rem/y	$\mu - 2\sigma \geq 40$	Yes
	12	UZr	8	2 rem/y	$\mu - 2\sigma \geq 40$	Yes

Table 4.6:   Testing scenarios and their corresponding constraints.

Physics-DES Integration

In order to estimate effective dose to fuel fabrication workers, the dose rate results from MCNP6.2 discussed in the previous chapter must be integrated into the ExtendSim models. This is achieved by building the dose rate outputs generated from MCNP6.2 into the foundation of the ExtendSim models (Figure 4.6).
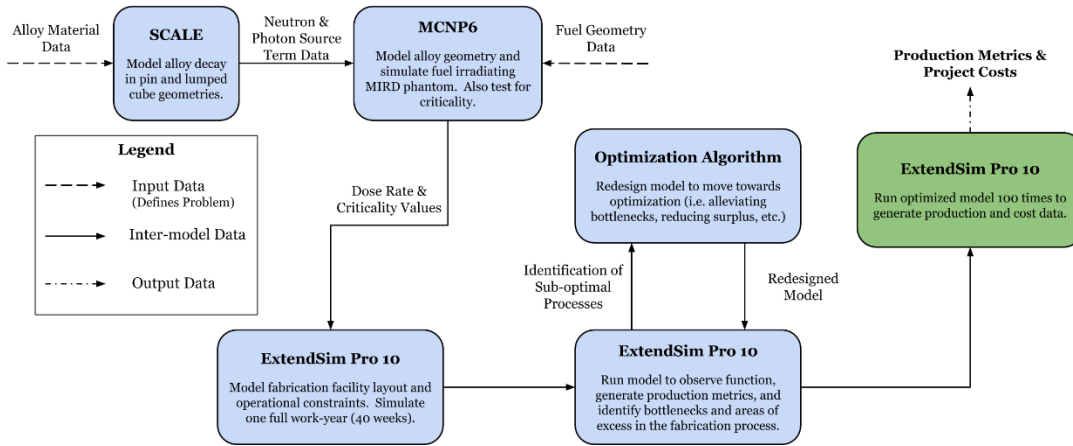
Figure 4.6:   Overview of SCALE-MCNP-ExtendSim coupling system.

As the DES model is being constructed, dose rate data is applied via a "constant" block which outputs a given numeric value that can be manipulated and utilized in a variety of mathematical functions. In the context of this thesis, activities in the DES model which simulate employees handling fuel in a given alloy-geometry configuration are coupled with "constant" blocks which outputs the corresponding dose rate for said alloy-geometry configuration (Tables 4.7 & 4.8).

Task	Effective Dose Rate, $\dot{E}$ (mrem/h)		
	UZr	UPuAmZr-0.03	UPuAmZr-0.6
Weigh Alloy	2.72×10^{-2}	1.17×10^{0}	1.08×10^{1}
Load/Unload Furnace	2.72×10^{-2}	1.17×10^{0}	1.08×10^{1}
Crush Heel	6.08×10^{-2}	1.87×10^{0}	1.87×10^{1}
Inspect Cast Pins	6.08×10^{-2}	1.87×10^{0}	1.87×10^{1}
Demold Cast Pins	6.08×10^{-2}	1.87×10^{0}	1.87×10^{1}
Measure Cast Pins	6.08×10^{-2}	1.87×10^{0}	1.87×10^{1}
Cut Cast Pins	6.08×10^{-2}	1.87×10^{0}	1.87×10^{1}
Inspect Cut Pins	6.08×10^{-2}	1.87×10^{0}	1.87×10^{1}
Load/Unload Jackets	5.58×10^{-2}	1.54×10^{0}	1.32×10^{1}
Weld Jackets	5.58×10^{-2}	1.54×10^{0}	1.32×10^{1}
Un-weld Jackets	5.58×10^{-2}	1.54×10^{0}	1.32×10^{1}
Bond & Inspect	2.38×10^{-1}	6.85×10^{0}	5.54×10^{1}
De-bond	2.38×10^{-1}	6.85×10^{0}	5.54×10^{1}
Final Inspection	2.38×10^{-1}	6.85×10^{0}	5.54×10^{1}

Table 4.7: Dose rate inputs for processes requiring the handling of fuel materials in non-consolidated configurations (Scenarios 1-10).

| Task | Effective Dose Rates, $\dot{E}$ (mrem/h) | |
	UZr	UPuAmZr-0.03
Weigh Alloy	0.0272	1.17
Load/Unload Furnace	0.0272	1.17
Crush Heel	0.0481	1.23
Inspect Cast Pins	0.169	5.30
Demold Cast Pins	0.0792	2.31
Measure Cast Pins	0.0792	2.31
Cut Cast Pins	0.0792	2.31
Inspect Cut Pins	0.169	4.89
Load/Unload Jackets	0.243	6.99
Weld Jackets	0.305	8.97
Un-weld Jackets	0.305	8.97
Bond & Inspect	0.441	13.3
De-bond	0.390	11.7
Final Inspection	0.390	11.7

Table 4.8:   Dose rate inputs for processes requiring the handling of fuel materials in consolidated glove box configurations (Scenarios 11 & 12).

During simulations, any time a fuel-handling activity block is active (i.e. a task is actively being performed), an output signal of 1 is sent to an "integrate" block via an information connector (illustrated as the "Up Time" label in Figure 13). Likewise, while an activity block is inactive, an output value of 0 is transmitted. Over the entire 6,720 simulated hours the model runs for, the "integrate" block records the value conveyed by the "Up Time" connector and integrates the resulting curve to find the total amount of time the activity was being performed in units of minutes, $T_{total,i}$. Next, the active time value is converted to units of hours. This is accomplished by utilizing a "math" block, which takes information steams from two or more blocks and performs mathematical functions with the values it receives. In context of the dose recording process, the integrated time value, $T_{total,i}$, and a value of 60, originating from a "constant" block, are input into the "math" block as the dividend and the divisor, respectively. The outcome of this process is a total

activity time in units of hours. Following this, a similar process is conducted in which the total activity time is multiplied by an hourly dose rate, $\dot{E}_i$, provided by the aforementioned dose rate "constant" block which was created alongside the "activity" block in question. The resulting output of the "math" block is the total dose imparted across all personnel from that single task, E_i.
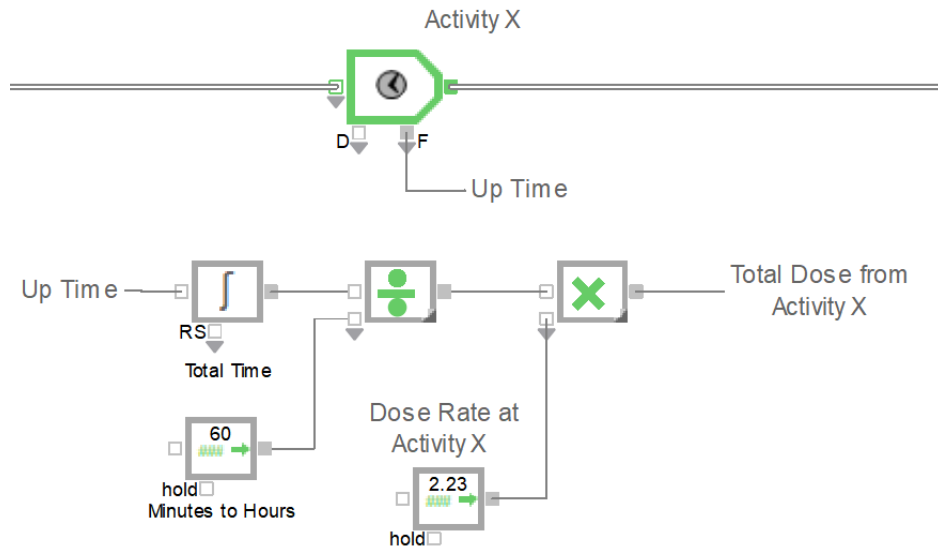
Figure 4.7:   Illustration of dose rate-DES integration.

Determining the effective dose to individual employees is a post-facto process that occurs after simulations have been run and is calculated by considering three factors: the value of the dose limit design constraint, L, the total dose burden of the MNF fabrication process imparted to a given class of employee from all relevant tasks, E_{tot}^j, and the number of employees of said classification needed to optimally staff the production of fuel pins, n_j. As described by Eq. 4.1, the average dose to individual employees, $\bar{E}_j$, is simply the total dose burden, E_{tot}^j, divided by the optimal staffing count, n_j, times the number of

redundancy hires needed to ensure no individual surpasses their annual dose limit, L (a variation on Eq. 3.2).

$$\bar{E}_j = \frac{E_{tot}^j}{\left\lceil \frac{\left[E_{tot}^j/n_j\right]}{L} \right\rceil \cdot n_j}$$

Eq. 4.1

COST ESTIMATIONS

The total equivalent costs of the VTR are calculated via a relatively simplistic summation of four categorical costs: material costs, infrastructure investments, employee wages, and overhead expenditures.

The first of these categories, infrastructure, represents a one-time, initial purchase which is required to outfit the MNF fabrication facility with the needed equipment and machinery to facility fuel assembly fabrication. Representative prices used in this thesis for glove boxes [46], welding stations, and other necessary machines and structures are presented in Tables 4.9 & 4.10.

Unit	Price	Footprint
Casting Glove Box	$8,800,000.00	59.38 ft^2
Handling Glove Box	$5,650,000.00	59.38 ft^2
Prepping Glove Box	$5,650,000.00	59.38 ft^2
Casting Chamber	$2,000,000.00	-
Vacuum Pump	-	9.66 ft^2
Mold Removal Apparatus	$100,000.00	-
Inspection Station	$200,000.00	-
Pin Cutter	$100,000.00	-
Welding Station	$500,000.00	-
Pin Prep. Area	$100,000.00	-
He Leak Checker	$100,000.00	-

Table 4.9:   Pin production-related infrastructure costs.

Unit	Price	Footprint
Na-Bonding Lane	$100,000.00	-
Na-Extrusion Device	$100,000.00	-
Jacket Cutting Station	$1,370.00	20.25 ft^2
Jacket Bending Station	$5,100.00	20.25 ft^2
Jacket Welding Station	$10,000.00	20.25 ft^2
Jacket Inspection Station	-	20.25 ft^2
Crucible Coating Station	$6,686.00	19.41 ft^2
Crucible Oven	$2,160.00	19.41 ft^2
Vycor Coating Station	$6,686.00	19.41 ft^2
Vycor Oven	$2,160.00	19.41 ft^2
Vycor Inspection Station	-	19.41 ft^2

Table 4.10: Non-pin production-related infrastructure costs.

Material expenses represent purchases that must be made periodically throughout the operation of the MNF fabrication process in order to adequately supply subsystems with their needed components. Materials such as metallic sodium, Vycor molds, and type 304 SS are substances which can be bought in bulk from commercial vendors. The prices of such items were chosen to reflect wholesale market rates. Specialty items, such as the sub-assembly components, were assigned assumed unit prices, as market prices for such items are not widely available. Finally, the cost of the fuel alloys is set to reflect the mean price of similar MNF [47].

Material	Cost
Fuel Alloy	$20,000.00 / kg
Metallic Sodium	$3.04 / kg
Vycor Mold	$30.70 / unit
Y_2O_3	$1,580.00 / kg
Graphite Crucible	$290.00 / unit
Type 304 SS	$236.00 / m^2
Sub-Assembly Ends	$1,000 / unit
Sub-Assembly Grids	$1,000 / unit

Table 4.11: Representative input values for material costs.

As mentioned in previous sections, employees are given two distinct classifications in the DES models. However, in terms of wages and pay, both welders and general laborers are assigned an equivalent employee cost: $22/h [48]. The total cost incurred by employee wages throughout the lifetime of the VTR project is simply given as the product of the total hours worked by both groups of workers and their hourly wage summed over ten years.

Overhead expenses include several external costs that arise from the need to support employees in non-pin fabrication related fields, including office leases, employee benefits, and supervisors' salaries [49]. This cost is approximated by simply multiplying the total cost of wages by a factor of 5.

Overall, the cost of the VTR project will be assessed by its total equivalent cost, C. Assuming a program lifetime of 10 years and an annual inflation rate of 2.27%, this total can be calculated with

$$C = \sum_{i=0}^{9} \left[\sum_{j} M_j m_j f_j + (1 + OM) \cdot \sum_{l} (W_l w_l \cdot 1{,}600) \right] \cdot 1.0227^i + \sum_{k} R_k r_k \qquad \textit{Eq. 4.2}$$

Variable		Meaning
Exogenous	M_j	Material type, j
	m_j	Per-unit cost of material, j
	w_l	Wage of worker class, l
	OM	Overhead multiplier
	R_k	Units of infrastructure, k
	r_k	Per-unit cost of infrastructure, k
Endogenous	f_j	Frequency of purchase of material, j
	W_l	Number of workers in class, l

Table 4.12:   Variable definitions for VTR lifetime cost equation.

UNCERTAINTY

In DES models, uncertainty is integrated into the "activity" blocks that define the system via their processing time, failure rate, and recovery time distributions [32]. Additionally, uncertainty is also incorporated into the pass:fail ratios that define the various inspection processes throughout the fabrication process. Given that the system being modeled contains over 100 processes governed by probabilistic behaviors and is executed over approximately 10^6 distinct time steps, the complexity of this system prevents uncertainty propagation from being analytically determined [50]. As such, uncertainty measurements must be determined using the results generated by the models in a *post facto* manner.

RESULTS

To generate cost, production, and dose rate estimations for evaluation, each of the 12 DES models is run 100 times. This quantity was chosen as it would provide ample data points to adequately characterize the distribution of outcomes each model could produce while also being fast enough to run as to not incur excessive computational expenses (nominally, 2 hours per 100 runs).

Lifetime and Monthly Costs

As detailed in Figure 15, lifetime costs for the VTR program are highly sensitive to changes in design constraint values, exhibiting average lifetime program expenses ranging from $717.7M to $827.4M. The highest of these lifetime costs occur when design constraints stipulate that the UPuAmZr-0.6 alloy is to be employed as the working fuel; in both Scenarios 3 & 6 (scenarios in which the UPuAmZr-0.6 alloy is employed), program costs rise in excess of $824M, a 6.40% increase over the baseline configuration (Scenario 2). Similarly, Scenarios 7 & 8, configurations in which dose limits are reduced to 0.5 rem/y also incur increased program costs, reaching totals of $795.2M and $791.2M, respectively.

Conversely, scenarios in which scheduling, infrastructure demands, and production reliability standards are adjusted and/or relaxed yield savings relative to our baseline configuration. These effects, detailed in Table 4.13, range from marginal to significant; adopting a 4-10 work schedule returns savings of just $4.0M. Meanwhile, lowering production throughput confidence and allowing for consolidated glove box operations reduce total equivalent cost of the VTR by $43.3 and $40.0M, respectively.
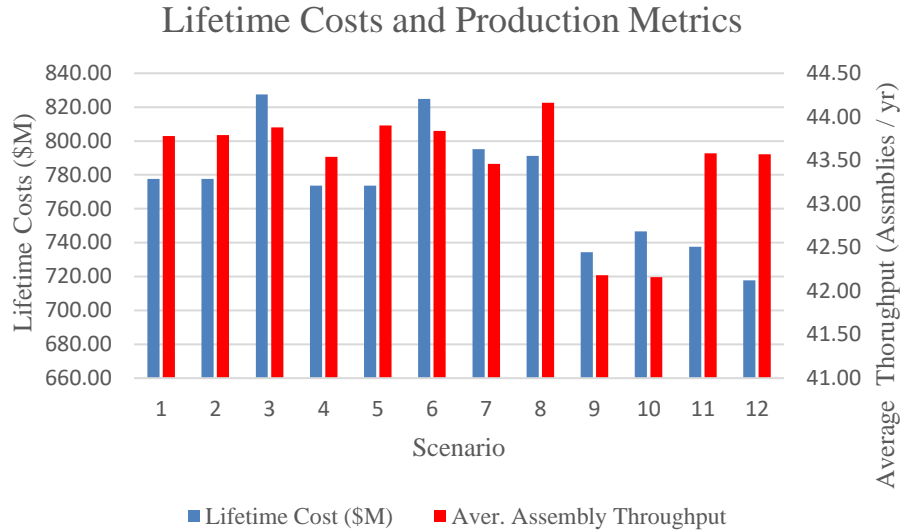
Figure 4.8:   Total equivalent costs of the VTR fuel fabrication facility and throughput metrics by scenario.

Design Constraint	Lifetime Cost ($M)			
	Minimum	Maximum	Change (-/+)	% Change (-/+)
Alloy	777.7	827.4	0 / 49.8	0 / 6.40
Schedule	773.7	777.7	-4.0 / 0	-0.51 / 0
Dose Limit	777.7	795.2	0 / 17.6	0 / 2.26
Production Confidence	734.3	777.7	-43.3 / 0	-5.57 / 0
Consolidation	737.6	777.7	-40.0 / 0	-5.15 / 0

Table 4.13:   Project lifetime cost changes due to changes in single design constraints relative to Scenario 2.

Examining program costs in terms of their monthly categorical costs reveals that recurring materials purchases dominate total project expenses. As illustrated in Figures 4.9 & 4.10, materials expenses account for anywhere between 73% and 85% of total monthly costs. Conversely, when annuitized to reflect monthly equivalent costs, infrastructure accounts for only 9% to 17% of said expenses. Employee wages and overhead, in turn, contribute a maximum of 11% to the total monthly equivalent total.

These findings support the results tabulated in Table 4.13; scenarios which lessen production demands (i.e. Scenarios 9 & 10) lead to reductions in materials demands, thereby reducing the impact of the largest cost contributor.
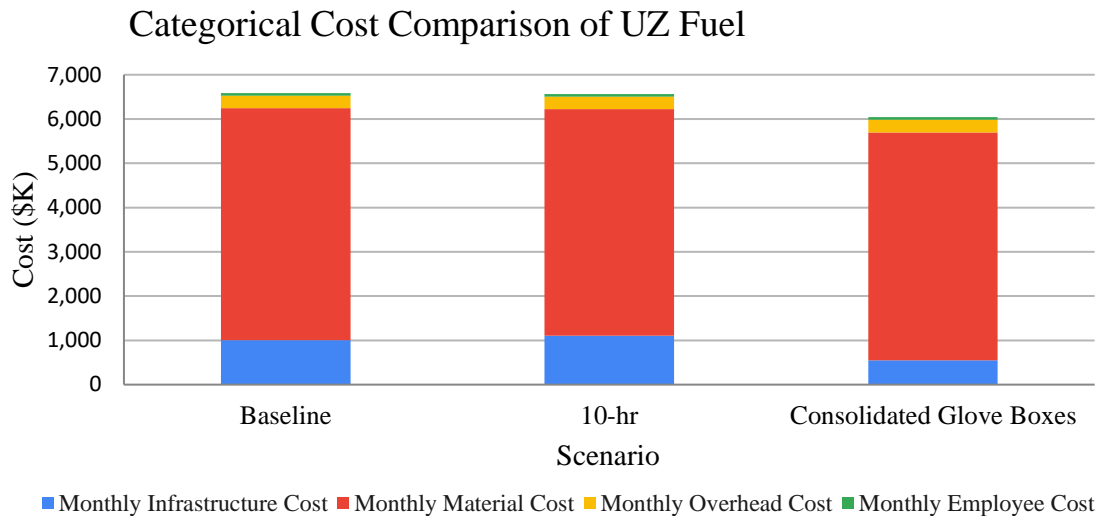
Figure 4.9:   Cost breakdown by category for scenarios employing UZr fuel.
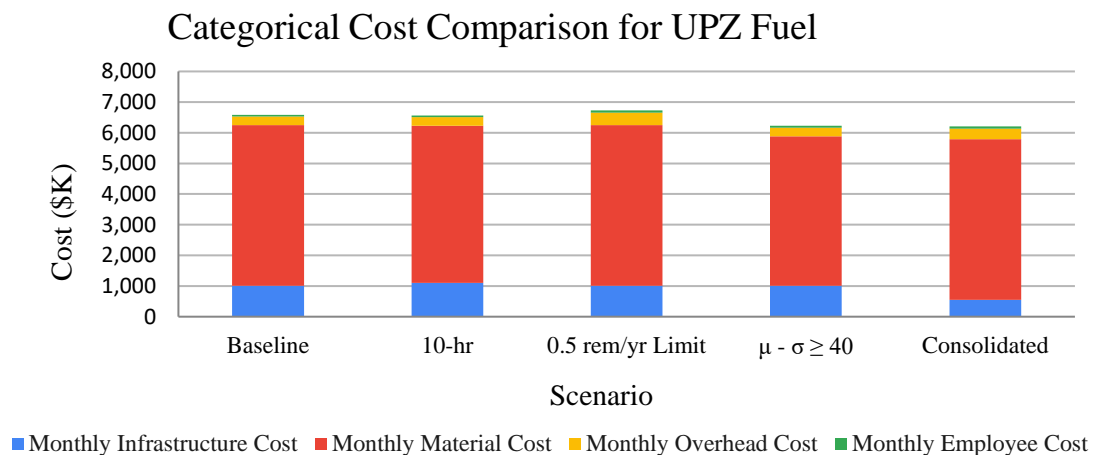
Figure 4.10: Cost breakdown by category for scenarios employing UPuAmZr-0.03 fuel.

Fuel Assembly Production

Fuel assembly production metrics respond subtlety as changes in design constraints are applied. As illustrated in Figure 4.8 and detailed in Table 4.14, average assembly production throughput assumes values between 42.16 and 44.16 assemblies/y, a 4.63% difference across all scenarios. In all cases, average throughput satisfies the 40 assemblies/y constraint and average throughput values follow normal distributions (see Figures F.1-F.12). However, in order to satisfy the production target with 95% confidence, the MNF fabrication facility must overshoot their production goals by as much as 10.4%. This suggests that increased manufacturing reliability could be a mechanism for reducing cost, as limiting the number of excess assemblies produced would decrease material and employee costs.

Scenario No.	Average Throughput, μ	Std. Dev., σ	Per-Assembly Cost ($K)
Scenario 1	43.78	1.33	1,805.6
Scenario 2	43.79	1.37	1,805.2
Scenario 3	43.88	1.40	1,914.9
Scenario 4	43.54	1.82	1,809.4
Scenario 5	43.90	1.59	1,794.6
Scenario 6	43.84	1.56	1,913.9
Scenario 7	43.46	1.65	1,859.3
Scenario 8	44.16	1.60	1,823.8
Scenario 9	42.18	1.29	1,771.4
Scenario 10	42.16	1.77	1,804.7
Scenario 11	43.58	1.49	1,708.6
Scenario 12	43.57	1.62	1,663.4

Table 4.14: Average annual fuel assembly throughput and standard deviation values for each scenario.

Facility Footprint

The spatial constraint of fitting the MNF fabrication facility within existing INL infrastructure proves to be a non-binding constraint; as detailed in Table 4.15, all of the 12 models developed can fit within an area of 2,352.67 ft^2. With an assumed 1.5 ft buffer zone around each station, the entire MNF fabrication facility could be constructed and operated within the FMF and ZPPR.

Scenario No.	Footprint (ft^2)
Scenario 1	2,230.18
Scenario 2	2,230.18
Scenario 3	2,230.18
Scenario 4	2,312.68
Scenario 5	2,312.68
Scenario 6	2,312.68
Scenario 7	2,230.18
Scenario 8	2,312.68
Scenario 9	2,230.18
Scenario 10	2,150.68
Scenario 11	1,691.38
Scenario 12	1,691.38

Table 4.15:   Feasible MNF fabrication facility footprints.

Additional space could be saved if non-fuel handling processes, such as jacket fabrication and subassembly hardware assembly, could be outsourced.

Effective Dose Rates

Figure 18 illustrates the average annual effective dose workers will receive when working under each of the 12 scenarios explored before redundancy hires are made to reduce individuals' dose rates below the 2,000 mrem/y limit. Across all configurations, annual effective dose rates for general labor assume values spanning three orders of

magnitude, ranging from 32.68 to 13,238.31 mrem/y. Similarly, the average dose rates to welders ranges from 43.29 to 23,755.70 mrem/y.

Average Annual Dose by Scenario
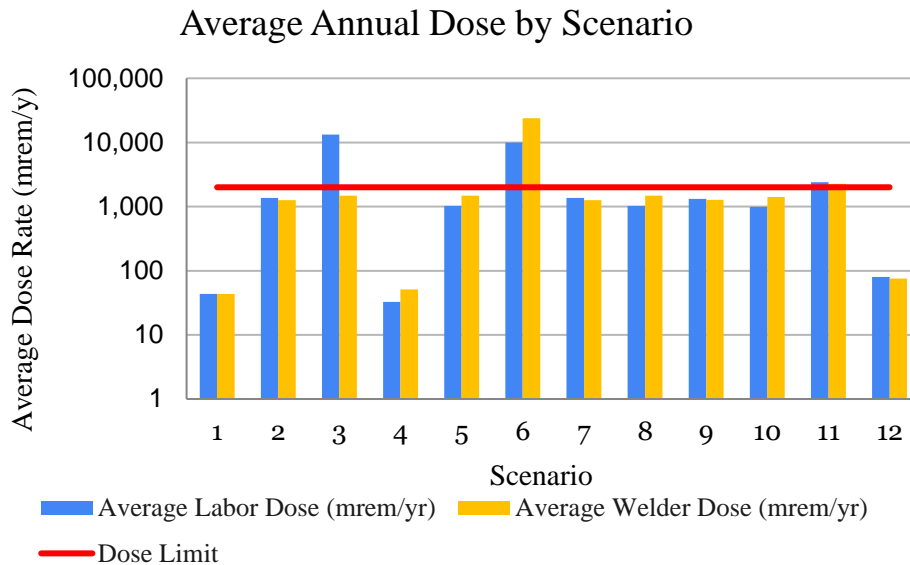
Figure 4.11: Average dose to personnel by job and scenario plotted on semi-log scale.

As expected, scenarios which employ UZr as the working fuel deliver effective annual dose rates that are approximately one and two orders of magnitude below their UPuAmZr-0.03 and UPuAmZr-0.6 counterparts; across all UZr-employing scenarios, annual effective dose rates fail to rise above 79.72 mrem/y for both general labor and welders, meaning redundancy hiring will not be required if UZr fuels are utilized.

In contrast, the selection of UPuAmZr-0.03 only requires redundancy hiring in three scenarios: Scenarios 7, 8, and 11. In these circumstances where dose limits are lowered (i.e. Scenarios 7 & 8), annual dose rates range from 1,028.85 to 1,479.35 mrem/y, requiring a tripling in staffing requirements. Likewise, in Scenario 11, where glove box operations are spatially consolidated, dose rates reach 2,401.37 mrem/y for general laborers and 2,252.60 mrem/y for welders. This results in staffing requirements needing to be

doubled in order to comply with the 2,000 mrem/y limit. The number of workers required under each scenario is detailed in Table 4.16.

Scenario No.	No. of General Labor	No. of Welders	Total Personnel
1	17	11	28
2	17	11	28
3	41	21	62
4	17	11	28
5	17	11	28
6	42	21	63
7	25	15	40
8	25	15	40
9	17	11	28
10	16	11	27
11	21	13	34
12	17	11	28

Table 4.16:   Minimum number of workers required by facility configuration.

Uncertainty Propagation

Applying a 10% uncertainty to all categorical costs can vary the overall lifetime program cost by as much as ±8.61%. As detailed in Table 4.17, uncertainty in material costs introduces the largest uncertainty into our lifetime costs calculations, followed by infrastructure cost uncertainty and then wages uncertainty. These findings indicate that the overall VTR program costs are highly sensitive to fluctuations in material costs. Conversely, variations in employee wages and infrastructure investment prices have marginal influence on the overall VTR program costs; a 10% change in these parameters result in an average lifetime cost uncertainty of ±1.35% and ±0.68%, respectively.

Additionally, while dose rates derived from MCNP6.2 simulations did embody small levels of uncertainty, the impact of this uncertainty is negligible in comparison to the

effects described above. Dose rate error of the likes described in Chapter III would manifest itself as modest increases or decreases in the average dose absorbed by workers, none of which would result in any change to redundancy hires. As such, dose rate errors do not noticeably contribute to the overall uncertainty of the DES models, and can therefore be ignored.

	Scenario No.	Cost Category Uncertainty Propagation		
		Infrastructure	Materials	Wages
Alloy Variation	1	±1.39 %	±8.08 %	±0.53 %
	2	±1.39 %	±8.08 %	±0.53 %
	3	±1.39 %	±7.60 %	±1.10 %
4-10 Schedule	4	±1.54 %	±7.93 %	±0.53 %
	5	±1.54 %	±7.93 %	±0.53 %
	6	±1.44 %	±7.44 %	±1.12 %
Strict Dose Limit	7	±1.36 %	±7.91 %	±0.74 %
	8	±1.50 %	±7.76 %	±0.74 %
Lowered Confidence	9	±1.47 %	±7.97 %	±0.56 %
	10	±1.59 %	±7.88 %	±0.53 %
Consolidated Operations	11	±0.80 %	±8.53 %	±0.67 %
	12	±0.80 %	±8.61 %	±0.57 %

Table 4.17: Uncertainty in project lifetime costs due to 10% uncertainty in cost inputs.

Chapter V: Conclusion

For the VTR program to supply the VTR with MNF using facilities at INL, significant investments will need to be made, both in terms of initial infrastructure purchases and on-going operating expenses. However, with careful selection of fuel-alloy composition and operation policies, an MNF fabrication facility can be optimized to minimize cost while simultaneously satisfying production demands and adhering to safety requirements. In examining the results generated by the 12 models built as part of this thesis, not only can we estimate what an optimized facility looks like and how it operates, but we can also extract key insights into how design variables choices drive project costs.

Figure 5.1 depicts the final, optimized design of a baseline fuel fabrication facility. To produce a minimum of 40 fuel assemblies per year with a confidence exceeding 95%, and to keep employee effective doses below 2 rem/y, the following personnel and infrastructure will be required:

Personnel / Infrastructure	Minimum Requirements
Welders	11
General Labor	17
Pin Casting Lanes	3
Jacket Production Lanes	4
Na-Bonding Lanes	3
Crucible & Vycor Production Lanes	2
Glove Boxes	16

Table 5.1: Baseline facility configuration personnel and infrastructure requirements.

In this configuration, the facility produces an average of 43.79 finished fuel assemblies per work-year, meeting its 40 assemblies per year production goal with 95% confidence. This, in turn, incurs a monthly equivalent cost of $6.587M. In all explored

configuration, infrastructure investments dominate total costs; material, overhead, and then employee on-going expenses contribute to overall project costs in order of diminishing significance. In terms of dose burden, welders will absorb an average 1,261.11 mrem/y while general laborers will absorb an average of 1,358.44 mrem/y. In both cases, neither class of worker will reach their dose limits, and therefore no redundancy hires will be required. Overall, this configuration would incur a lifetime cost of $ 777.658M assuming a 2.27% annual inflation rate.

Figure 5.1:   Optimized fuel fabrication facility configuration.

79

However, if design constraints can be adjusted to lower total equivalent costs, one can reduce the lifetime total by $43.309M – a 5.57% decrease. As depicted in Table 4.13, allowing either the production confidence constraint or consolidated glove box constraint to be relaxed yields savings in the form of reduced material purchasing and/or reduced infrastructure needs. Shifting operations to a 4-10 schedule yields could potentially result in modest savings, reducing lifetime costs by roughly $3.978M. However, this option would incur the consequence of needing to purchase extra infrastructure (an additional pin casting lane). Conversely, lowering dose limits to 0.5 rem/y strictly leads to significant increases, adding as much as $ 17.563M to the lifetime project investment. These increased costs stem from the need to make redundancy hires in order to be dose limit-compliant. Additionally, while not explored in this study, outsourcing jacket, crucible, and/or Vycor production could further lower project costs, as in eliminating these jobs would reduce both infrastructure and personnel needs.

Overall, to craft a safe, cost-optimized MNF fabrication facility, INL should consider adjusting their historic facility designs and operational policies to reflect the configuration modeled in Scenarios 9, 11, or 12. In each of these cases, MNF production occurs under a 5-8 schedule in consolidated glove boxes. Additionally, workers would be limited to an annual effective dose of 2 rem/y and the facility will aim to meet minimum production goals with a minimum of 68.3% confidence. These configurations would require the following:

| | Minimum Requirements | | |
Personnel / Infrastructure	Scenario 9	Scenario 11	Scenario 12
Welders	11	13	11
General Labor	17	21	17
Pin Casting Lanes	3	3	3
Jacket Production Lanes	4	4	4
Na-Bonding Lanes	3	3	3
Crucible & Vycor Production Lanes	2	2	2
Glove Boxes	16	9	9

Table 5.2:   Facility configuration, personnel, and infrastructure requirements for Scenarios 11 & 12.

While configuring a facility to resemble Scenario 9 would yield significant savings over its Scenario 2 counterpart, the reduced production confidence could potentially lead to situations in which INL cannot independently supply the VTR with enough fuel to remain operational. This could be detrimental to the success of the VTR program, so a careful risk analysis should be performed before this option is seriously considered.

Ultimately, this thesis posits that Scenario 11 is the most attractive MNF fabrication facility candidate design. Despite requiring a minimum of two persons being hired for each job to be in compliance with dose limits (which would incur increased overhead and employee costs), the lowered cost due to reduced glove box demands more than offsets the personnel expenses, all while meeting minimum reliability, throughput, and safety requirements. Additionally, while not within the scope of this study, the consequences of employing alloys containing transuranic isotopes may be compensated by the benefits of removing both plutonium and nuclear waste from the fuel cycle. The operators of the VTR program could be financially rewarded for burning these waste products in the VTR. Depending on the monetary value of this tradeoff, the utilization of UPuAmZr-0.03 in lieu of UZr fuel could be an equitable, if not favorable, less-expensive configuration.

Appendix A: MCNP6.2 Model Diagrams
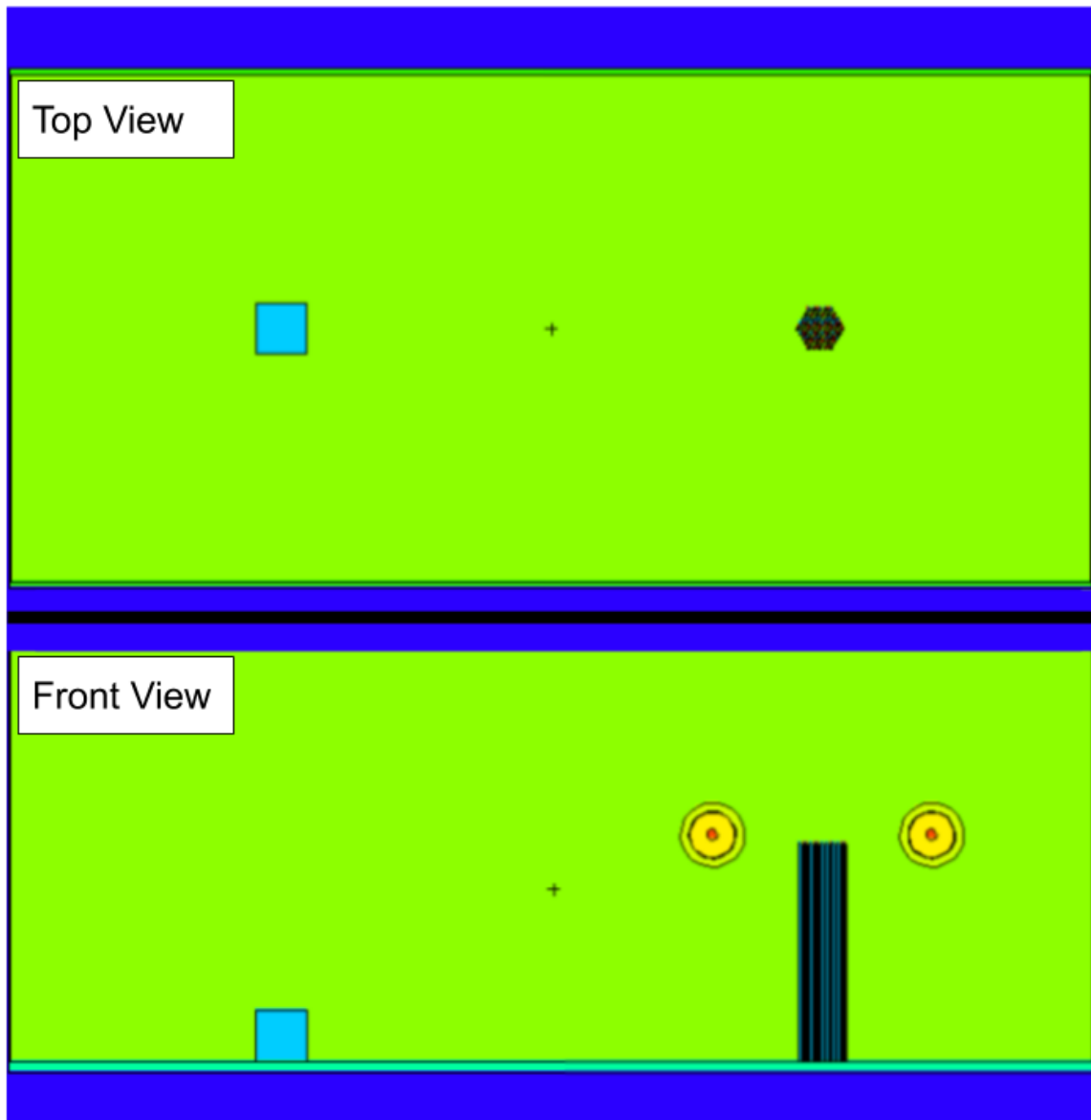
Figure A.1: Illustration of the lumped cube-cast pin array configuration using MCNPX Visual Editor.
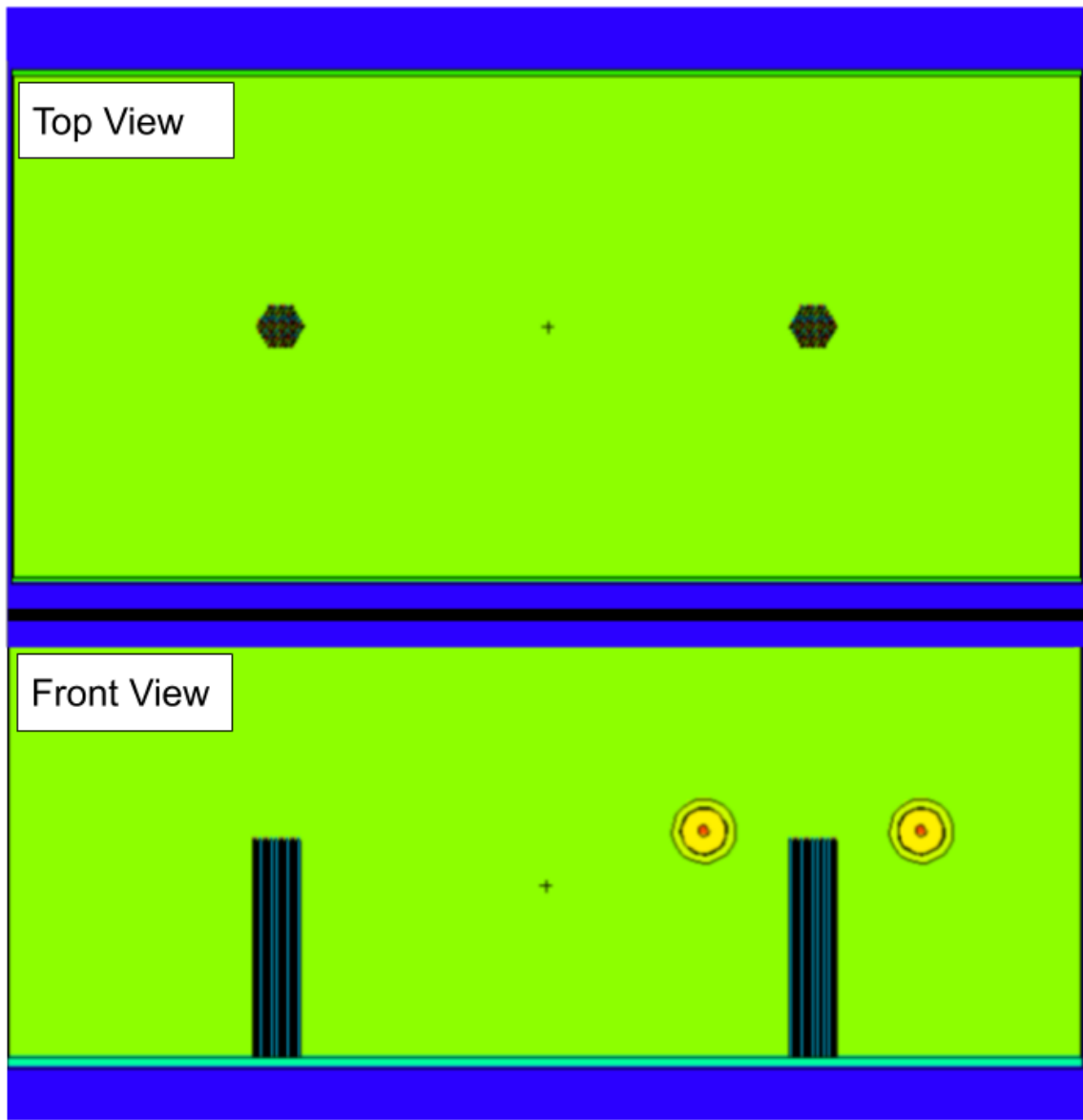
Figure A.2: Illustration of the two cast pin array configuration using MCNPX Visual Editor.
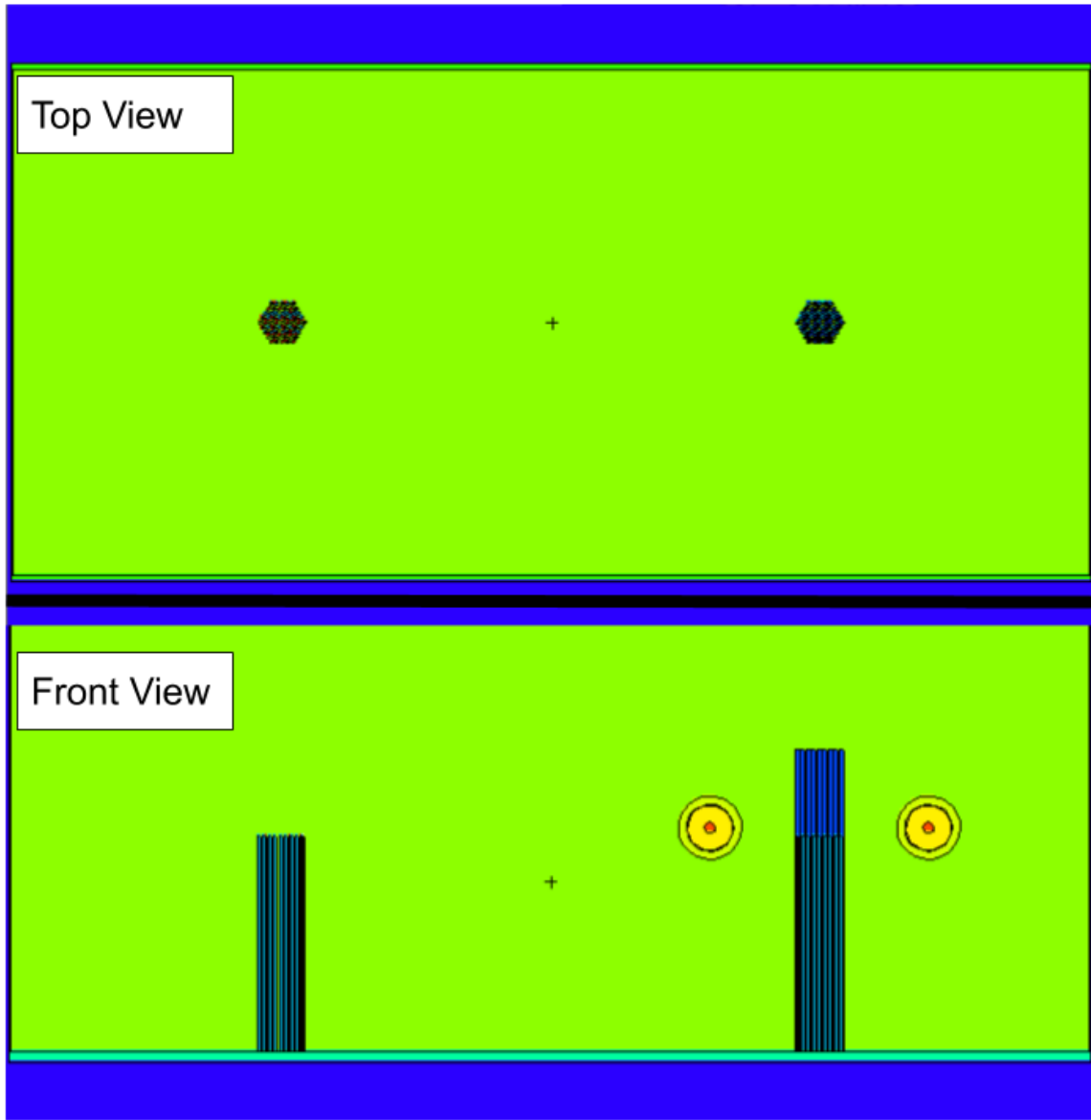
Figure A.3: Illustration of the cast pin array-finished pin array configuration using MCNPX Visual Editor.
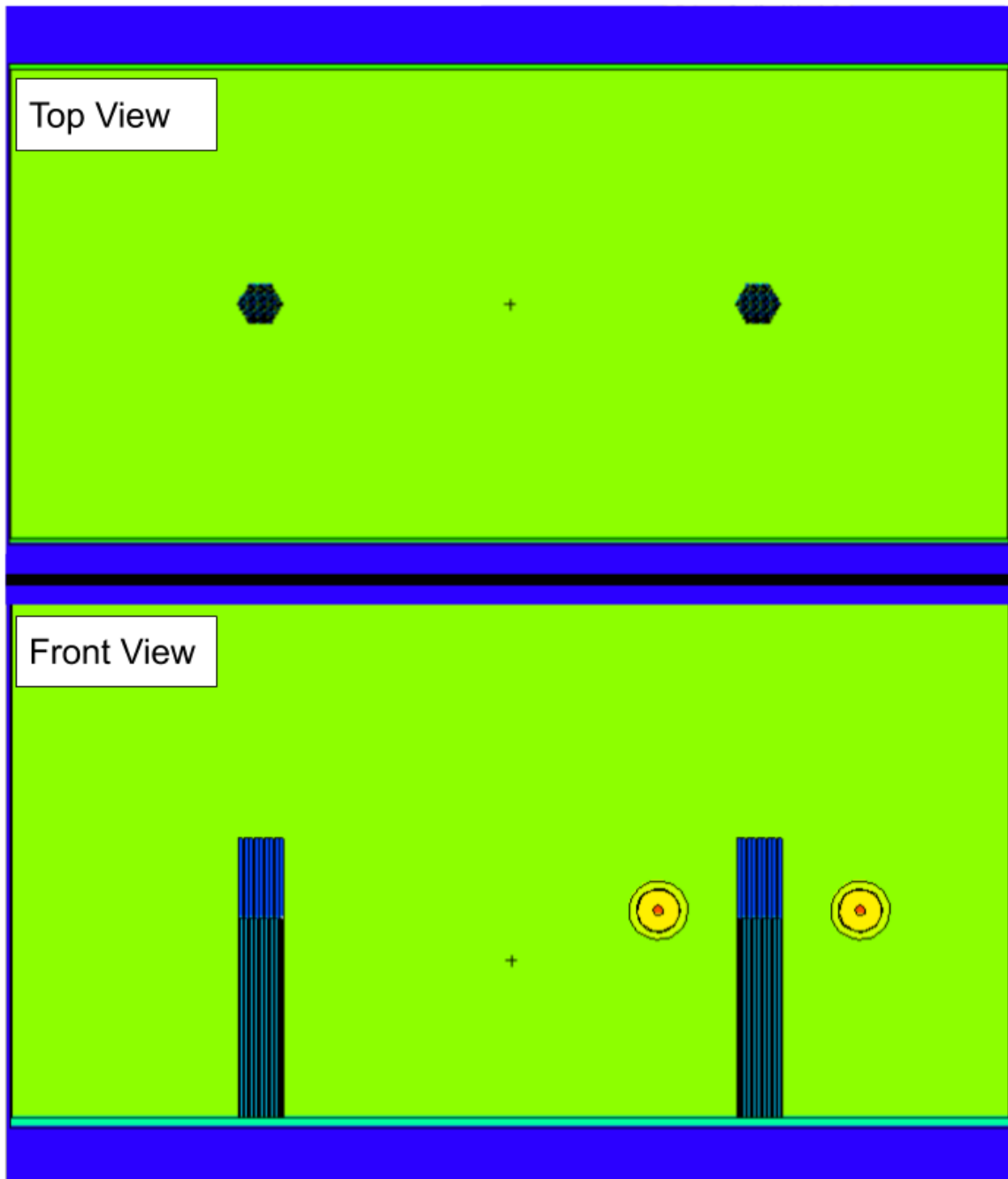
Figure A.4: Illustration of the two finished pin arrays configuration using MCNPX Visual Editor.
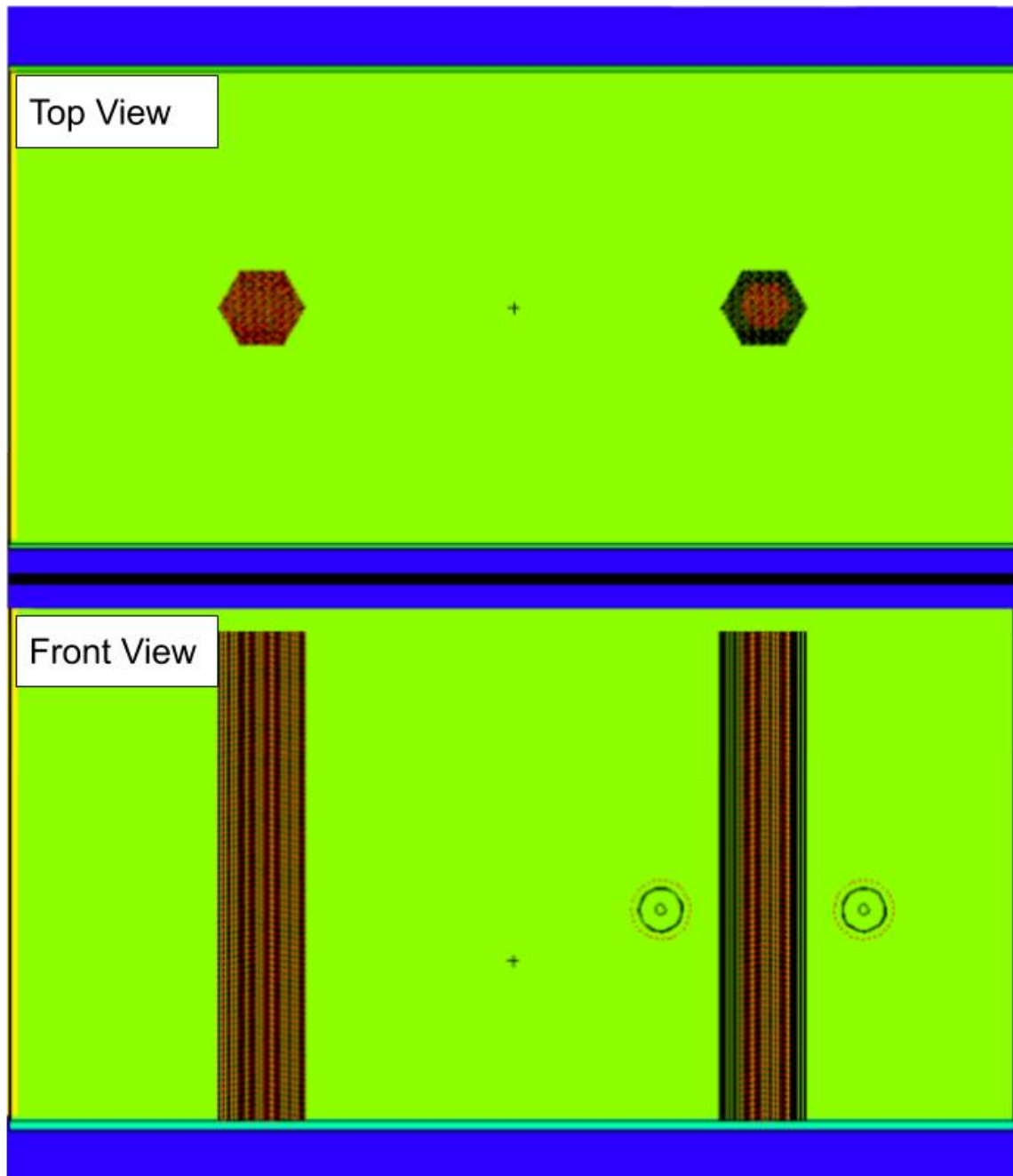
Figure A.6: Illustration of the two fuel assemblies configuration using MCNPX Visual Editor.
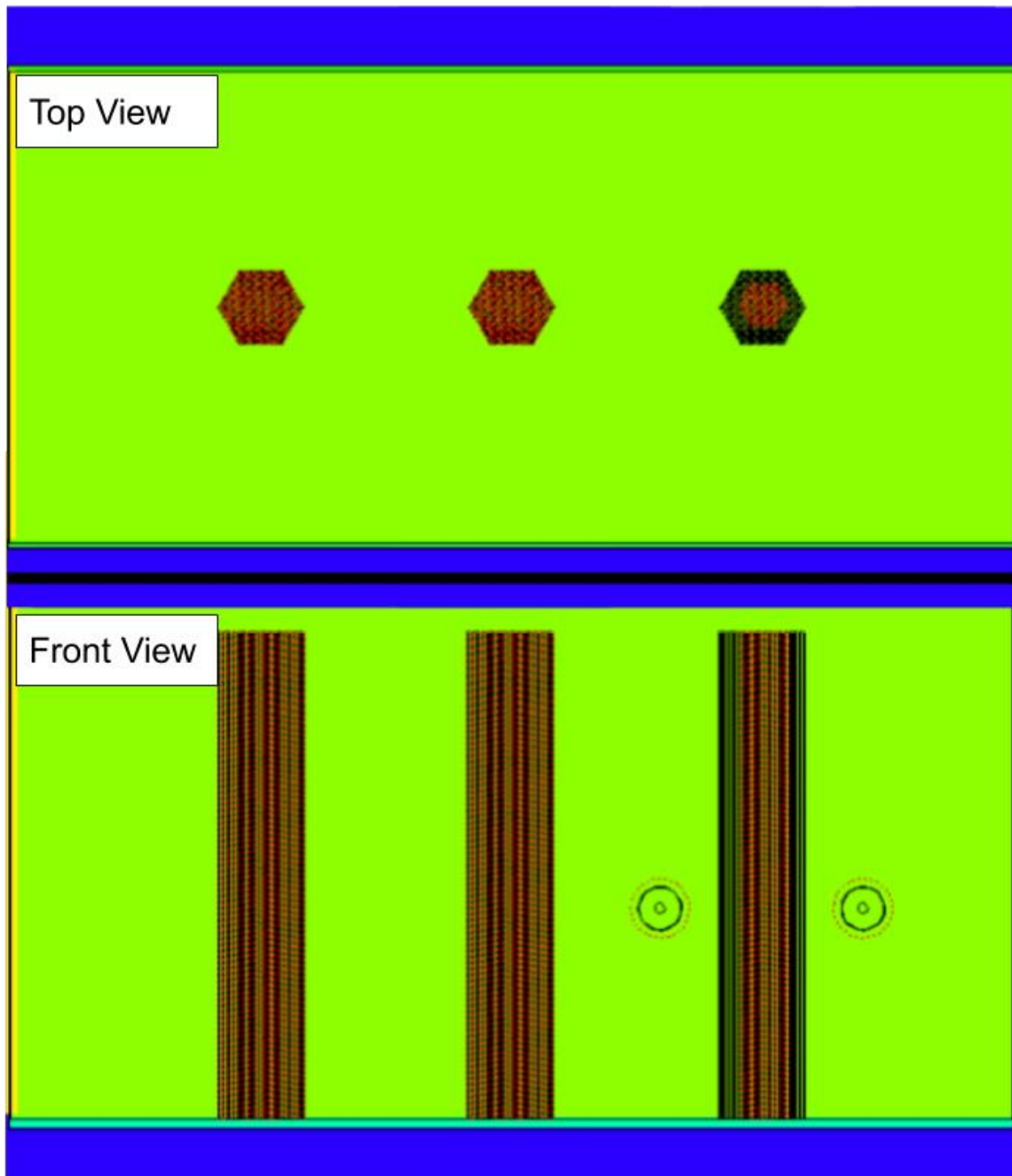
Figure A.7: Illustration of the three fuel assemblies configuration using MCNPX Visual Editor.

Appendix B: ICRP Dose Coefficients

Neutron Energy (MeV)	Conversion Factor (mrem-cm^2)
$1.00\text{x}10^{-9}$	$5.24\text{x}10^{-7}$
$1.00\text{x}10^{-8}$	$6.55\text{x}10^{-7}$
$2.50\text{x}10^{-8}$	$7.60\text{x}10^{-7}$
$1.00\text{x}10^{-7}$	$9.95\text{x}10^{-7}$
$2.00\text{x}10^{-7}$	$1.12\text{x}10^{-6}$
$5.00\text{x}10^{-7}$	$1.28\text{x}10^{-6}$
$1.00\text{x}10^{-6}$	$1.38\text{x}10^{-6}$
$2.00\text{x}10^{-6}$	$1.45\text{x}10^{-6}$
$5.00\text{x}10^{-6}$	$1.50\text{x}10^{-6}$
$1.00\text{x}10^{-5}$	$1.51\text{x}10^{-6}$
$2.00\text{x}10^{-5}$	$1.51\text{x}10^{-6}$
$5.00\text{x}10^{-5}$	$1.48\text{x}10^{-6}$
$1.00\text{x}10^{-4}$	$1.46\text{x}10^{-6}$
$2.00\text{x}10^{-4}$	$1.44\text{x}10^{-6}$
$5.00\text{x}10^{-4}$	$1.42\text{x}10^{-6}$
$1.00\text{x}10^{-3}$	$1.42\text{x}10^{-6}$
$2.00\text{x}10^{-3}$	$1.44\text{x}10^{-6}$
$5.00\text{x}10^{-3}$	$1.57\text{x}10^{-6}$
$1.00\text{x}10^{-2}$	$1.83\text{x}10^{-6}$
$2.00\text{x}10^{-2}$	$2.38\text{x}10^{-6}$
$3.00\text{x}10^{-2}$	$2.90\text{x}10^{-6}$
$5.00\text{x}10^{-2}$	$3.85\text{x}10^{-6}$
$7.00\text{x}10^{-2}$	$4.72\text{x}10^{-6}$
$1.00\text{x}10^{-1}$	$5.98\text{x}10^{-6}$
$1.50\text{x}10^{-1}$	$8.02\text{x}10^{-6}$
$2.00\text{x}10^{-1}$	$9.90\text{x}10^{-6}$
$3.00\text{x}10^{-1}$	$1.33\text{x}10^{-4}$
$5.00\text{x}10^{-1}$	$1.88\text{x}10^{-4}$
$7.00\text{x}10^{-1}$	$2.31\text{x}10^{-4}$
$9.00\text{x}10^{-1}$	$2.67\text{x}10^{-4}$
$1.00\text{x}10^{+0}$	$2.82\text{x}10^{-4}$

Table B.1:   Neutron dose coefficients [21]

Photon Energy (MeV)	Conversion Factor (mrem-cm^2)
1.00×10^{-2}	4.96×10^{-9}
1.50×10^{-2}	1.29×10^{-8}
2.00×10^{-2}	2.11×10^{-8}
3.00×10^{-2}	3.07×10^{-8}
4.00×10^{-2}	3.45×10^{-8}
5.00×10^{-2}	3.64×10^{-8}
6.00×10^{-2}	3.83×10^{-8}
7.00×10^{-2}	4.19×10^{-8}
8.00×10^{-2}	4.40×10^{-8}
1.00×10^{-1}	5.17×10^{-8}
1.50×10^{-1}	7.56×10^{-8}
2.00×10^{-1}	1.00×10^{-7}
3.00×10^{-1}	1.50×10^{-7}
4.00×10^{-1}	2.00×10^{-7}
5.00×10^{-1}	2.48×10^{-7}
6.00×10^{-1}	2.90×10^{-7}
8.00×10^{-1}	3.73×10^{-7}
$1.00 \times 10^{+0}$	4.47×10^{-7}
$2.00 \times 10^{+0}$	7.45×10^{-7}
$4.00 \times 10^{+0}$	1.19×10^{-6}
$6.00 \times 10^{+0}$	1.57×10^{-6}
$8.00 \times 10^{+0}$	1.93×10^{-6}
$1.00 \times 10^{+1}$	2.30×10^{-6}

Table B.2:   Photon dose coefficients [21]

Appendix C: ORIGEN Tabulated Results

Alloy	Intensity at 0 d $\left(\frac{n}{s}\right)$	Intensity at 180 d $\left(\frac{n}{s}\right)$	Intensity at 365 d $\left(\frac{n}{s}\right)$	Difference Over Time (%)
UZr	5.08×10^{-1}	5.08×10^{-1}	5.08×10^{-1}	0.00
UPuAmZr-0.03	5.60×10^{6}	5.60×10^{2}	5.60×10^{2}	-0.01
UPuAmZr-0.6	5.59×10^{2}	5.59×10^{2}	5.59×10^{2}	-0.01

Table C.1:   Neutron intensity data for fuel pin geometries.

Alloy	Intensity at 0 d $\left(\frac{n}{s}\right)$	Intensity at 180 d $\left(\frac{n}{s}\right)$	Intensity at 365 d $\left(\frac{n}{s}\right)$	Difference Over Time (%)
UZr	5.16×10^{1}	5.16×10^{1}	5.16×10^{1}	0.00
UPuAmZr-0.03	5.70×10^{4}	5.70×10^{4}	5.70×10^{4}	-0.01
UPuAmZr-0.6	5.68×10^{4}	5.68×10^{4}	5.68×10^{4}	-0.01

Table C.2:   Neutron intensity data for lumped cube geometries.

Alloy	Intensity at 0 d $\left(\frac{\gamma}{s}\right)$	Intensity at 180 d $\left(\frac{n}{s}\right)$	Intensity at 365 d $\left(\frac{\gamma}{s}\right)$	Difference Over Time (%)
UZr	1.70×10^{6}	2.35×10^{6}	2.35×10^{6}	38.91
UPuAmZr-0.03	6.45×10^{9}	6.45×10^{9}	6.45×10^{9}	-0.15
UPuAmZr-0.6	6.80×10^{10}	6.79×10^{10}	6.79×10^{10}	-0.08

Table C.3:   Photon intensity data for fuel pin geometries.

Alloy	Intensity at 0 d $\left(\frac{\gamma}{s}\right)$	Intensity at 180 d $\left(\frac{n}{s}\right)$	Intensity at 365 d $\left(\frac{\gamma}{s}\right)$	Difference Over Time (%)
UZr	1.72×10^{8}	2.39×10^{8}	2.39×10^{8}	38.92
UPuAmZr-0.03	6.56×10^{11}	6.56×10^{11}	6.56×10^{11}	-0.15
UPuAmZr-0.6	6.91×10^{12}	6.90×10^{12}	6.90×10^{12}	-0.08

Table C.4:   Photon intensity data for lumped cube geometries.

Appendix D: Properties of Radionuclides

Isotope	Half-life (y)	Decay Constant (y^{-1})
^{234}U	2.455×10^5	4.073×10^{-6}
^{235}U	7.040×10^8	1.420×10^{-9}
^{236}U	2.342×10^7	4.270×10^{-8}
^{238}U	4.468×10^9	2.238×10^{-10}
^{239}Pu	2.411×10^4	4.148×10^{-5}
^{240}Pu	6.561×10^3	1.524×10^{-4}
^{241}Am	4.326×10^2	2.312×10^{-3}

Table D.1:   Half-life and decay constants of selected radionuclides [51]

Appendix E: MCNP6.2 Tabulated Results

CRITICALITY RESULTS

Alloy	k_{eff}	σ	$P(k_{eff} \leq x) = 0.99$
UZr	0.23696	0.00007	0.14983
UPuAmZr-0.03	0.36401	0.00009	0.36957
UPuAmZr-0.03 (H_2O)	0.56559	0.00023	0.56619
UPuAmZr-0.6	0.36023	0.00010	0.36567

Table E.1:   Criticality results for lumped cube geometries.

Alloy	k_{eff}	σ	$P(k_{eff} \leq x) = 0.99$
UZr	0.07466	0.00005	0.05063
UPuAmZr-0.03	0.10893	0.00006	0.10910
UPuAmZr-0.6	0.10816	0.00005	0.10808

Table E.2:   Criticality results for cast pin array geometries.

Alloy	k_{eff}	σ	$P(k_{eff} \leq x) = 0.99$
UZr	0.04985	0.00004	0.04995
UPuAmZr-0.03	0.10995	0.00005	0.11010
UPuAmZr-0.6	0.10886	0.00005	0.10899

Table E.3:   Criticality results for finished pin array geometries.

Alloy	k_{eff}	σ	$P(k_{eff} \leq x) = 0.99$
UZr	0.16104	0.00010	0.04995
UPuAmZr-0.03	0.22335	0.00010	0.11010
UPuAmZr-0.6	0.22105	0.00010	0.10899

Table E.4:   Criticality results for fuel assembly geometries.

Configuration	k_{eff}	σ	$P(k_{eff} \leq x) = 0.99$
Lumped Cube – Cast Pin Array	0.23704	0.00008	0.23725
Two Cast Pin Arrays	0.08341	0.00006	0.08357
Cast Pin Array – Finished Pin Array	0.08297	0.00006	0.08313
Two Finished Pin Arrays	0.08282	0.00006	0.08298
Two Fuel Assemblies	0.19316	0.00011	0.19347
Three Fuel Assemblies	0.22923	0.00014	0.22959

Table E.5:   Criticality results for consolidated glove box configurations utilizing UZr alloy.

Configuration	k_{eff}	σ	$P(k_{eff} \leq x) = 0.99$
Lumped Cube – Cast Pin Array	0.36379	0.00012	0.36409
Two Cast Pin Arrays	0.11755	0.00007	0.11774
Cast Pin Array – Finished Pin Array	0.11764	0.00007	0.11783
Two Finished Pin Arrays	0.11777	0.00007	0.11795
Two Fuel Assemblies	0.25635	0.00014	0.25672
Three Fuel Assemblies	0.29277	0.00013	0.29312

Table E.6:   Criticality results for consolidated glove box configurations utilizing UPuAmZr-0.03 alloy.

DOSE RATE RESULTS

Basic Geometric Configurations

Alloy	$\dot{E}_n(\frac{mrem}{h})$	$\varepsilon_n\ (\frac{mrem}{h})$	$\dot{E}_\gamma\ (\frac{mrem}{h})$	$\varepsilon_\gamma\ (\frac{mrem}{h})$	$\dot{E}_{total}\ (\frac{mrem}{h})$	$\varepsilon_{total}\ (\frac{mrem}{h})$	$\varepsilon_{total}\ (\%)$
UZr	2.52×10^{-4}	3.10×10^{-7}	2.70×10^{-2}	1.91×10^{-4}	2.72×10^{-2}	1.92×10^{-4}	0.70
UPuAmZr-0.03	3.68×10^{-1}	4.27×10^{-4}	7.97×10^{-1}	1.66×10^{-2}	$1.17\times10^{+0}$	1.70×10^{-2}	1.46
UPuAmZr-0.6	3.64×10^{-1}	4.25×10^{-4}	$1.04\times10^{+1}$	7.00×10^{-2}	$1.08\times10^{+1}$	7.04×10^{-2}	0.65

Table E.7:   Effective dose rates for lumped cube geometries.

Alloy	$\dot{E}_n(\frac{mrem}{h})$	$\varepsilon_n\ (\frac{mrem}{h})$	$\dot{E}_\gamma\ (\frac{mrem}{h})$	$\varepsilon_\gamma\ (\frac{mrem}{h})$	$\dot{E}_{total}\ (\frac{mrem}{h})$	$\varepsilon_{total}\ (\frac{mrem}{h})$	$\varepsilon_{total}\ (\%)$
UZr	1.67×10^{-4}	2.00×10^{-7}	6.06×10^{-2}	2.25×10^{-4}	6.08×10^{-2}	2.25×10^{-4}	0.37
UPuAmZr-0.03	2.24×10^{-1}	2.65×10^{-4}	1.65×10^{0}	1.52×10^{-2}	1.87×10^{0}	1.55×10^{-2}	0.83
UPuAmZr-0.6	2.23×10^{-1}	2.64×10^{-4}	1.85×10^{1}	8.44×10^{-2}	1.87×10^{1}	8.47×10^{-2}	0.45

Table E.8:   Effective dose rates for cast pin array geometries.

Alloy	$\dot{E}_n(\frac{mrem}{h})$	$\varepsilon_n\ (\frac{mrem}{h})$	$\dot{E}_\gamma\ (\frac{mrem}{h})$	$\varepsilon_\gamma\ (\frac{mrem}{h})$	$\dot{E}_{total}\ (\frac{mrem}{h})$	$\varepsilon_{total}\ (\frac{mrem}{h})$	ε_{total} (%)
UZr	1.66×10^{-4}	1.98×10^{-7}	5.56×10^{-2}	2.14×10^{-4}	5.58×10^{-2}	2.14×10^{-4}	0.38
UPuAmZr-0.03	2.22×10^{-1}	2.64×10^{-4}	1.32×10^{0}	1.65×10^{-2}	1.54×10^{0}	1.68×10^{-2}	1.09
UPuAmZr-0.6	2.22×10^{-1}	1.85×10^{-4}	1.29×10^{1}	9.60×10^{-2}	1.32×10^{1}	9.61×10^{-2}	0.73

Table E.9:   Effective dose rates for finished pin array geometries.

Alloy	$\dot{E}_n(\frac{mrem}{h})$	$\varepsilon_n\ (\frac{mrem}{h})$	$\dot{E}_\gamma\ (\frac{mrem}{h})$	$\varepsilon_\gamma\ (\frac{mrem}{h})$	$\dot{E}_{total}\ (\frac{mrem}{h})$	$\varepsilon_{total}\ (\frac{mrem}{h})$	ε_{total} (%)
UZr	1.12×10^{-3}	1.32×10^{-6}	2.37×10^{-1}	1.17×10^{-3}	2.38×10^{-1}	1.17×10^{-3}	0.49
UPuAmZr-0.03	1.54×10^{0}	1.78×10^{-3}	5.31×10^{0}	7.10×10^{-2}	6.85×10^{0}	7.28×10^{-2}	1.06
UPuAmZr-0.6	2.22×10^{-1}	1.85×10^{-4}	1.29×10^{1}	9.60×10^{-2}	1.32×10^{1}	9.61×10^{-2}	0.73

Table E.10: Effective dose rates for fuel assembly geometries.

Consolidated Configurations

Alloy	$\dot{E}_n(\frac{mrem}{h})$	$\varepsilon_n\ (\frac{mrem}{h})$	$\dot{E}_\gamma\ (\frac{mrem}{h})$	$\varepsilon_\gamma\ (\frac{mrem}{h})$	$\dot{E}_{total}\ (\frac{mrem}{h})$	$\varepsilon_{total}\ (\frac{mrem}{h})$	ε_{total} (%)
UZr	2.46×10^{-4}	3.55×10^{-7}	4.79×10^{-2}	3.17×10^{-4}	4.81×10^{-2}	3.17×10^{-4}	0.66
UPuAmZr-0.03	3.31×10^{-1}	4.73×10^{-4}	8.96×10^{-1}	2.30×10^{-2}	$1.23\times10^{+0}$	2.35×10^{-2}	1.91

Table E.11.1: Effective dose rates for lumped cube – cast pin array configurations.
Worker handling fuel in lumped cube geometry.

Alloy	$\dot{E}_n(\frac{mrem}{h})$	$\varepsilon_n\ (\frac{mrem}{h})$	$\dot{E}_\gamma\ (\frac{mrem}{h})$	$\varepsilon_\gamma\ (\frac{mrem}{h})$	$\dot{E}_{total}\ (\frac{mrem}{h})$	$\varepsilon_{total}\ (\frac{mrem}{h})$	ε_{total} (%)
UZr	4.45×10^{-4}	5.33×10^{-7}	1.68×10^{-1}	6.05×10^{-4}	1.69×10^{-1}	6.06×10^{-4}	0.36
UPuAmZr-0.03	5.97×10^{-1}	7.03×10^{-4}	$4.70\times10^{+0}$	4.17×10^{-2}	$5.30\times10^{+0}$	4.24×10^{-2}	0.80

Table E.11.2: Effective dose rates for lumped cube – cast pin array configurations.
Worker handling fuel in cast pin array geometry.

Alloy	$\dot{E}_n(\frac{mrem}{h})$	$\varepsilon_n (\frac{mrem}{h})$	$\dot{E}_\gamma (\frac{mrem}{h})$	$\varepsilon_\gamma (\frac{mrem}{h})$	$\dot{E}_{total} (\frac{mrem}{h})$	$\varepsilon_{total} (\frac{mrem}{h})$	ε_{total} (%)
UZr	2.60×10^{-4}	3.40×10^{-7}	7.90×10^{-2}	3.65×10^{-1}	7.92×10^{-2}	3.66×10^{-4}	0.46
UPuAmZr-0.03	3.48×10^{-1}	4.52×10^{-4}	$1.96\times10^{+0}$	2.45×10^{-2}	$2.31\times10^{+0}$	2.50×10^{-2}	1.08

Table E.12: Effective dose rates for two cast pin arrays configurations. Worker handling either cast pin array.

Alloy	$\dot{E}_n(\frac{mrem}{h})$	$\varepsilon_n (\frac{mrem}{h})$	$\dot{E}_\gamma (\frac{mrem}{h})$	$\varepsilon_\gamma (\frac{mrem}{h})$	$\dot{E}_{total} (\frac{mrem}{h})$	$\varepsilon_{total} (\frac{mrem}{h})$	ε_{total} (%)
UZr	2.60×10^{-4}	3.40×10^{-7}	7.68×10^{-2}	3.56×10^{-4}	7.70×10^{-2}	3.57×10^{-4}	0.46
UPuAmZr-0.03	3.48×10^{-1}	4.49×10^{-4}	1.89×10^{0}	2.31×10^{-2}	2.23×10^{0}	2.35×10^{-2}	1.05

Table E.13.1: Effective dose rates for cast pin array – finished pin array configurations. Worker handling fuel in cast pin array geometry.

Alloy	$\dot{E}_n(\frac{mrem}{h})$	$\varepsilon_n (\frac{mrem}{h})$	$\dot{E}_\gamma (\frac{mrem}{h})$	$\varepsilon_\gamma (\frac{mrem}{h})$	$\dot{E}_{total} (\frac{mrem}{h})$	$\varepsilon_{total} (\frac{mrem}{h})$	ε_{total} (%)
UZr	2.59×10^{-4}	3.38×10^{-7}	7.37×10^{-2}	3.54×10^{-4}	7.40×10^{-2}	3.54×10^{-4}	0.48
UPuAmZr-0.03	3.47×10^{-1}	4.48×10^{-4}	1.62×10^{0}	2.42×10^{-2}	1.96×10^{0}	2.47×10^{-2}	1.26

Table E.13.2: Effective dose rates for cast pin array – finished pin array configurations. Worker handling fuel in finished pin array geometry.

Alloy	$\dot{E}_n(\frac{mrem}{h})$	$\varepsilon_n (\frac{mrem}{h})$	$\dot{E}_\gamma (\frac{mrem}{h})$	$\varepsilon_\gamma (\frac{mrem}{h})$	$\dot{E}_{total} (\frac{mrem}{h})$	$\varepsilon_{total} (\frac{mrem}{h})$	ε_{total} (%)
UZr	2.58×10^{-4}	3.36×10^{-7}	7.24×10^{-2}	3.42×10^{-4}	7.26×10^{-2}	3.43×10^{-4}	0.47
UPuAmZr-0.03	3.48×10^{-1}	4.49×10^{-4}	1.49×10^{0}	2.19×10^{-2}	1.84×10^{0}	2.23×10^{-2}	1.21

Table 14:   Effective dose rates for two finished pin array configurations. Worker handling either array.

Alloy	$\dot{E}_n(\frac{mrem}{h})$	$\varepsilon_n (\frac{mrem}{h})$	$\dot{E}_\gamma (\frac{mrem}{h})$	$\varepsilon_\gamma (\frac{mrem}{h})$	$\dot{E}_{total} (\frac{mrem}{h})$	$\varepsilon_{total} (\frac{mrem}{h})$	ε_{total} (%)
UZr	1.82×10^{-3}	2.28×10^{-6}	3.03×10^{-1}	1.87×10^{-3}	3.05×10^{-1}	1.87×10^{-3}	0.61
UPuAmZr-0.03	$2.53\times10^{+0}$	3.11×10^{-3}	$6.44\times10^{+0}$	1.07×10^{-1}	$8.97\times10^{+0}$	1.10×10^{-1}	1.22

Table E.15: Effective dose rates for two fuel assemblies configurations. Worker handling either assembly.

Alloy	$\dot{E}_n(\frac{mrem}{h})$	$\varepsilon_n\ (\frac{mrem}{h})$	$\dot{E}_\gamma\ (\frac{mrem}{h})$	$\varepsilon_\gamma\ (\frac{mrem}{h})$	$\dot{E}_{total}\ (\frac{mrem}{h})$	$\varepsilon_{total}\ (\frac{mrem}{h})$	ε_{total} (%)
UZr	2.61×10^{-3}	3.30×10^{-6}	3.88×10^{-1}	2.61×10^{-3}	3.90×10^{-1}	2.62×10^{-3}	0.67
UPuAmZr-0.03	$3.45\times10^{+0}$	4.26×10^{-3}	$8.29\times10^{+0}$	1.78×10^{-1}	$1.17\times10^{+1}$	1.83×10^{-1}	1.56

Table E.16.1: Effective dose rates for three finished pin arrays configurations. Worker handling lateral finished pin arrays.

Alloy	$\dot{E}_n(\frac{mrem}{h})$	$\varepsilon_n\ (\frac{mrem}{h})$	$\dot{E}_\gamma\ (\frac{mrem}{h})$	$\varepsilon_\gamma\ (\frac{mrem}{h})$	$\dot{E}_{total}\ (\frac{mrem}{h})$	$\varepsilon_{total}\ (\frac{mrem}{h})$	ε_{total} (%)
UZr	2.82×10^{-3}	3.44×10^{-6}	4.38×10^{-1}	2.74×10^{-3}	4.41×10^{-1}	2.74×10^{-3}	0.62
UPuAmZr-0.03	$3.93\times10^{+0}$	4.63×10^{-3}	$9.33\times10^{+0}$	1.84×10^{-1}	$1.33\times10^{+1}$	1.89×10^{-1}	1.42

Table E.16.2: Effective dose rates for three finished pin arrays configurations. Worker handling central finished pin arrays.

Appendix F: ExtendSim Results
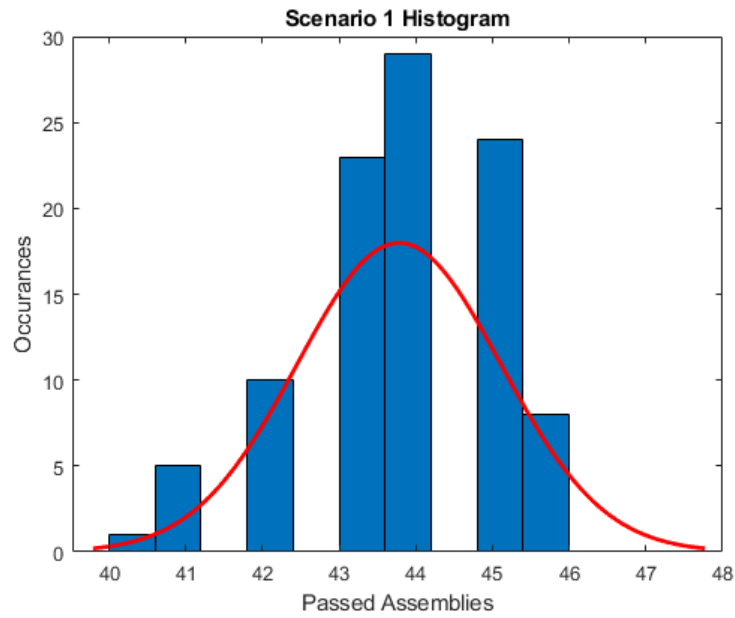
Figure F.1:   Histogram of passed assembly throughput for Scenario 1.
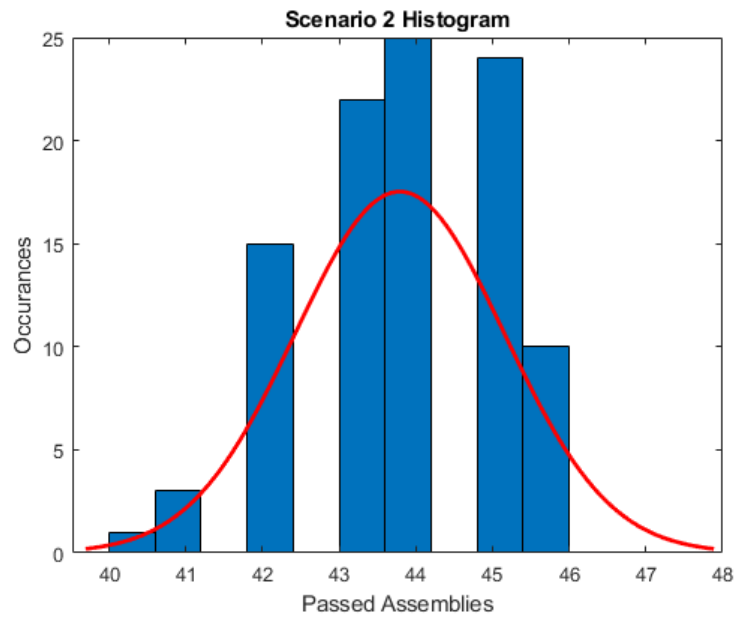
Figure F.2:   Histogram of passed assembly throughput for Scenario 2.
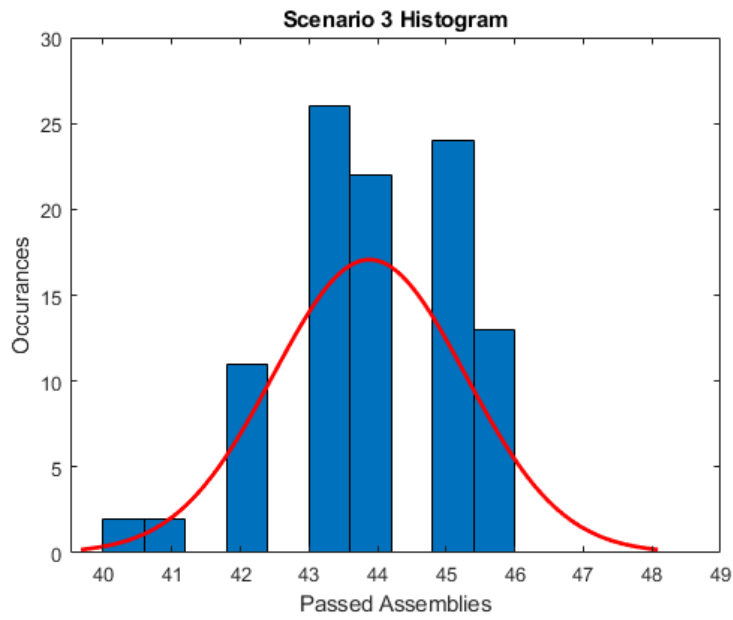
Figure F.3:   Histogram of passed assembly throughput for Scenario 3.
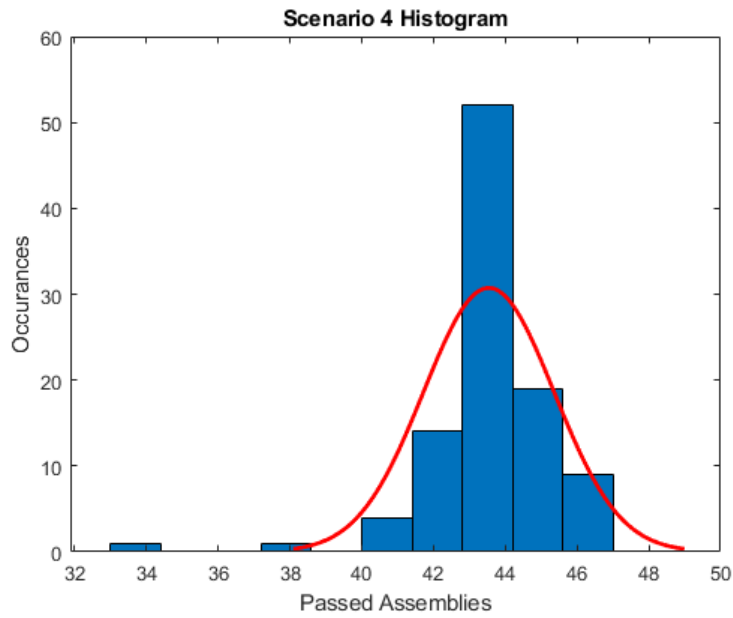
Figure F.4:   Histogram of passed assembly throughput for Scenario 4.
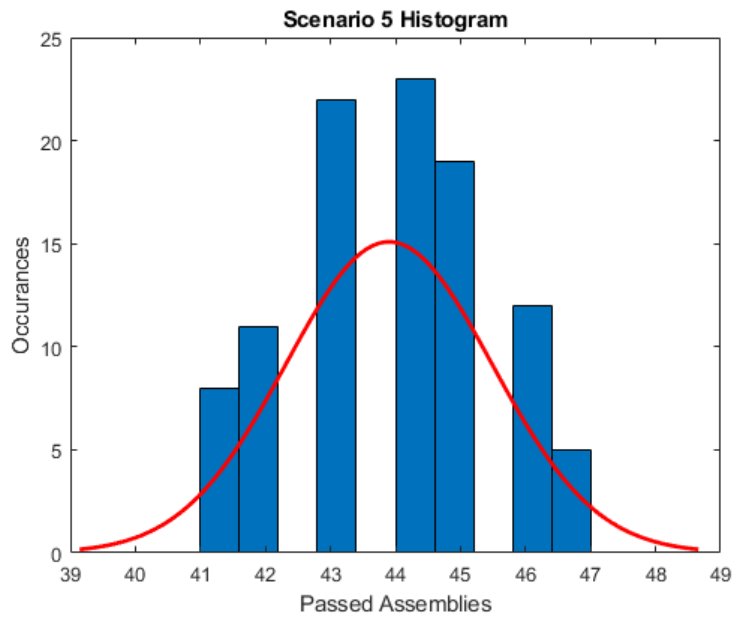
Figure F.5: Histogram of passed assembly throughput for Scenario 5.
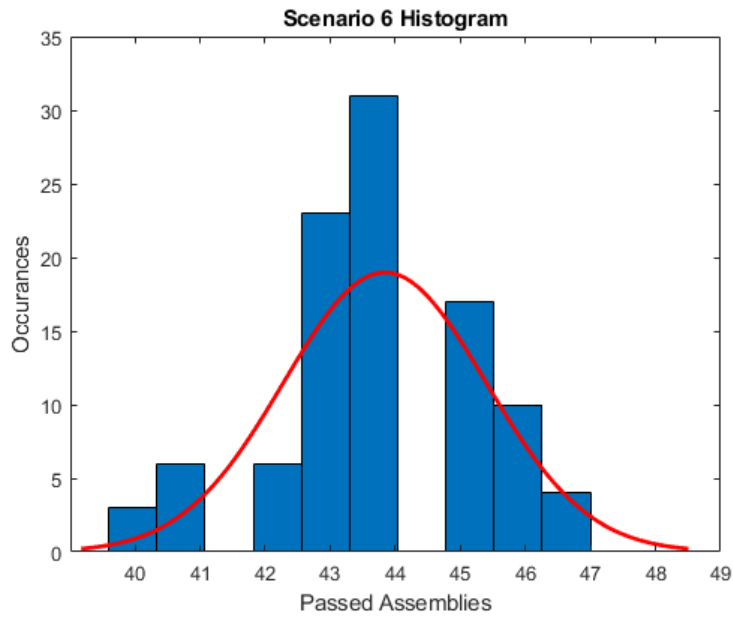
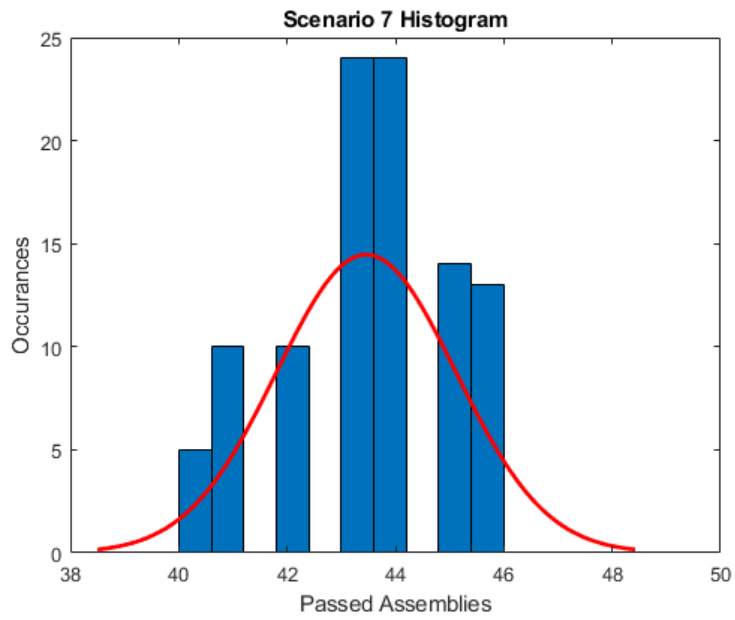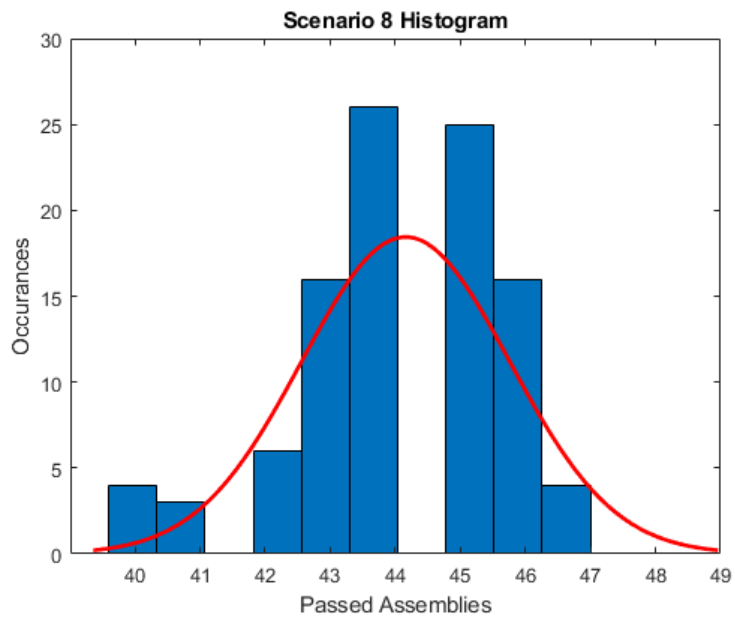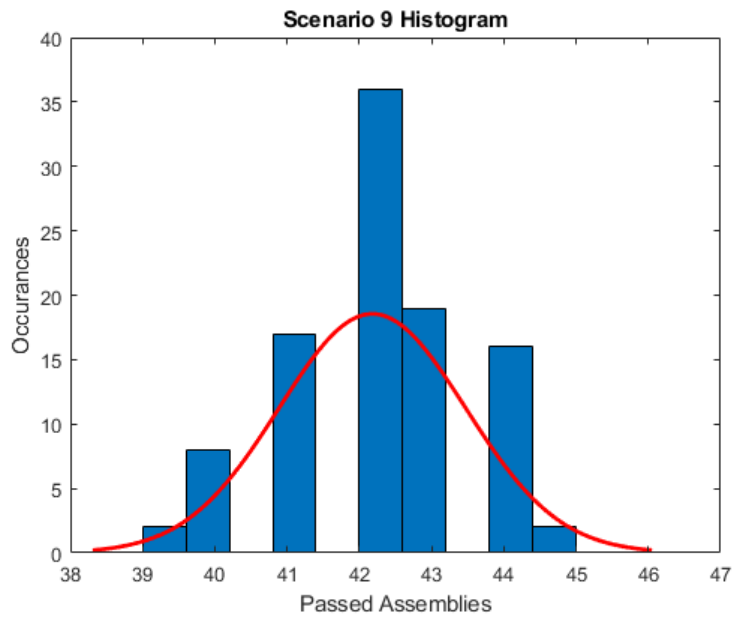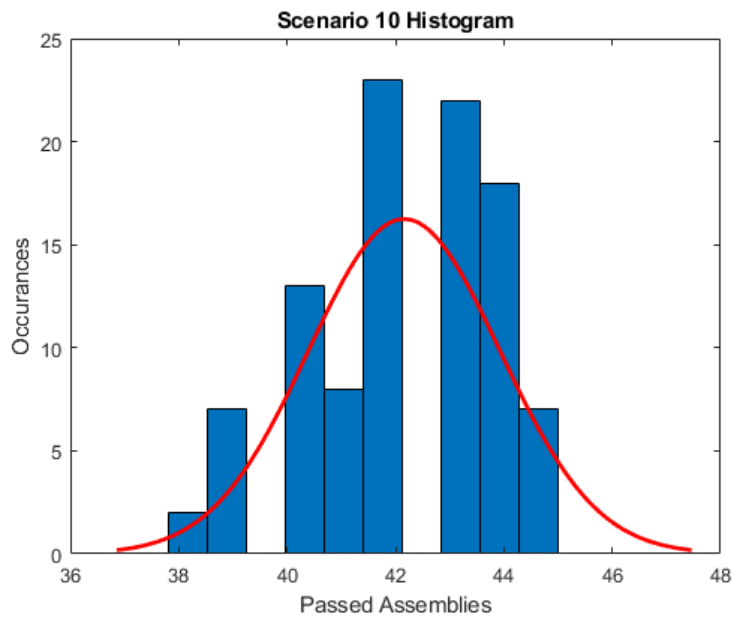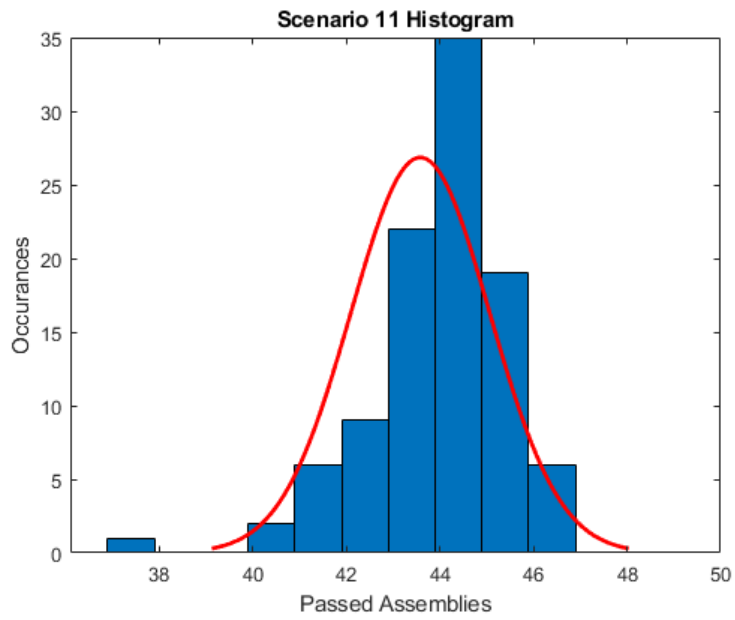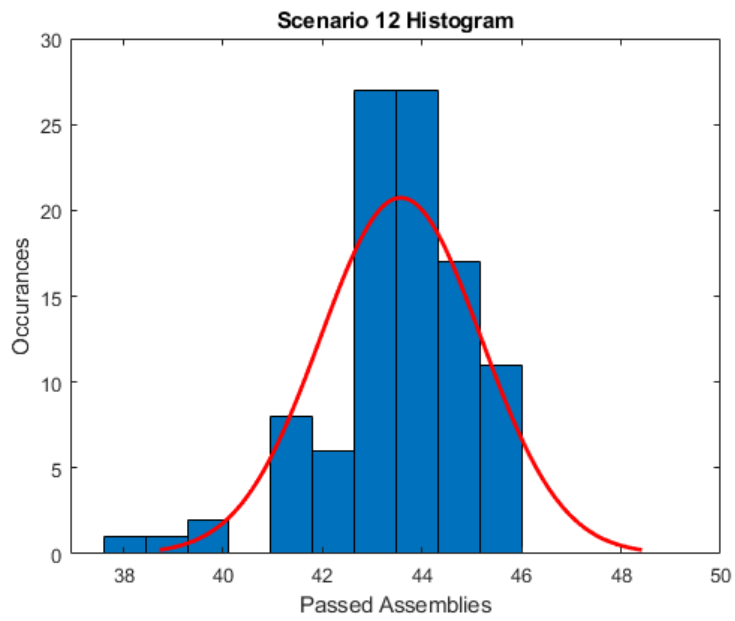Figure F.6: Histogram of passed assembly throughput for Scenario 6.

Figure F.7: Histogram of passed assembly throughput for Scenario 7.

Figure F.8: Histogram of passed assembly throughput for Scenario 8.

100

Figure F.9:   Histogram of passed assembly throughput for Scenario 9.

Figure F.10: Histogram of passed assembly throughput for Scenario 10.

Figure F.11: Histogram of passed assembly throughput for Scenario 11.

Figure F.12: Histogram of passed assembly throughput for Scenario 12.

Appendix G: ExtendSim Facility Models
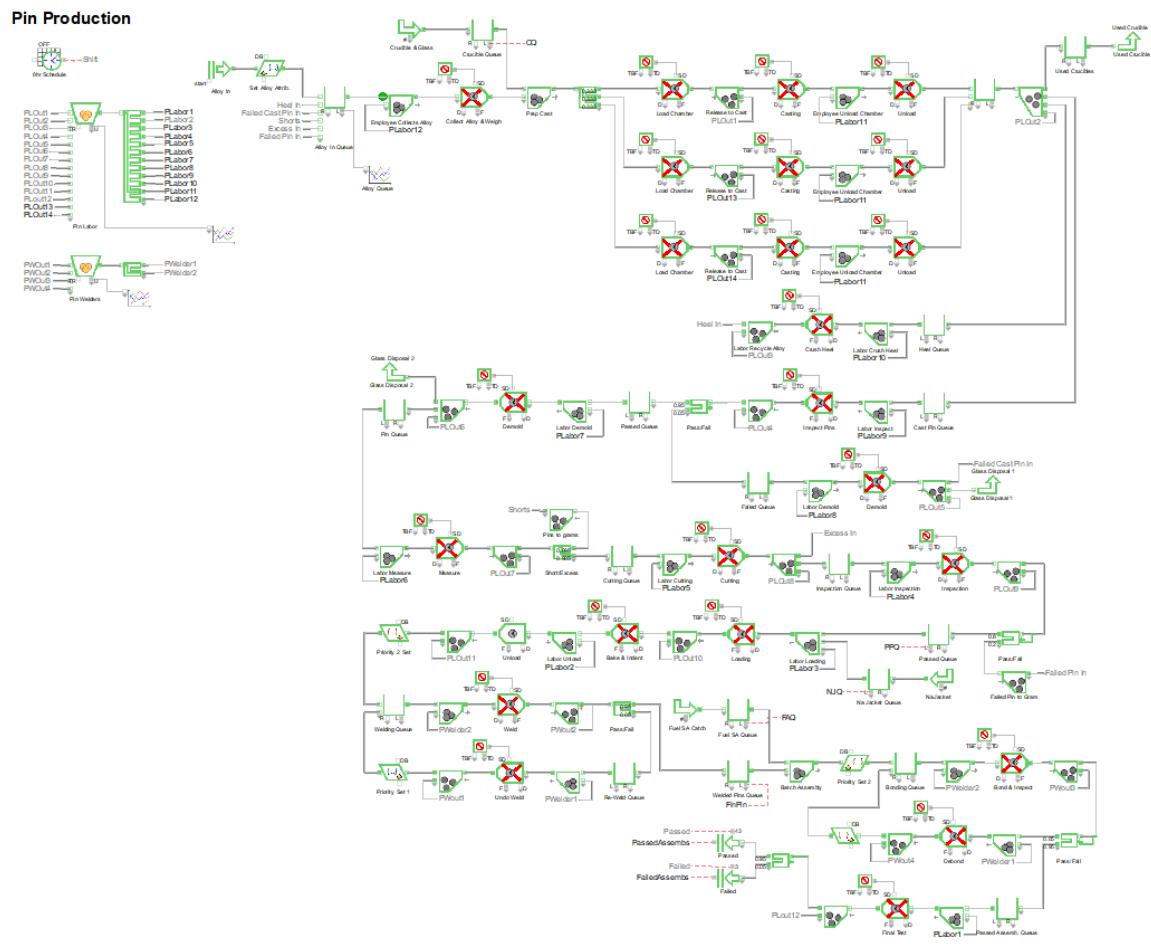
Figure G.1: Pin production subsystem model for 5-8 work week scenarios.
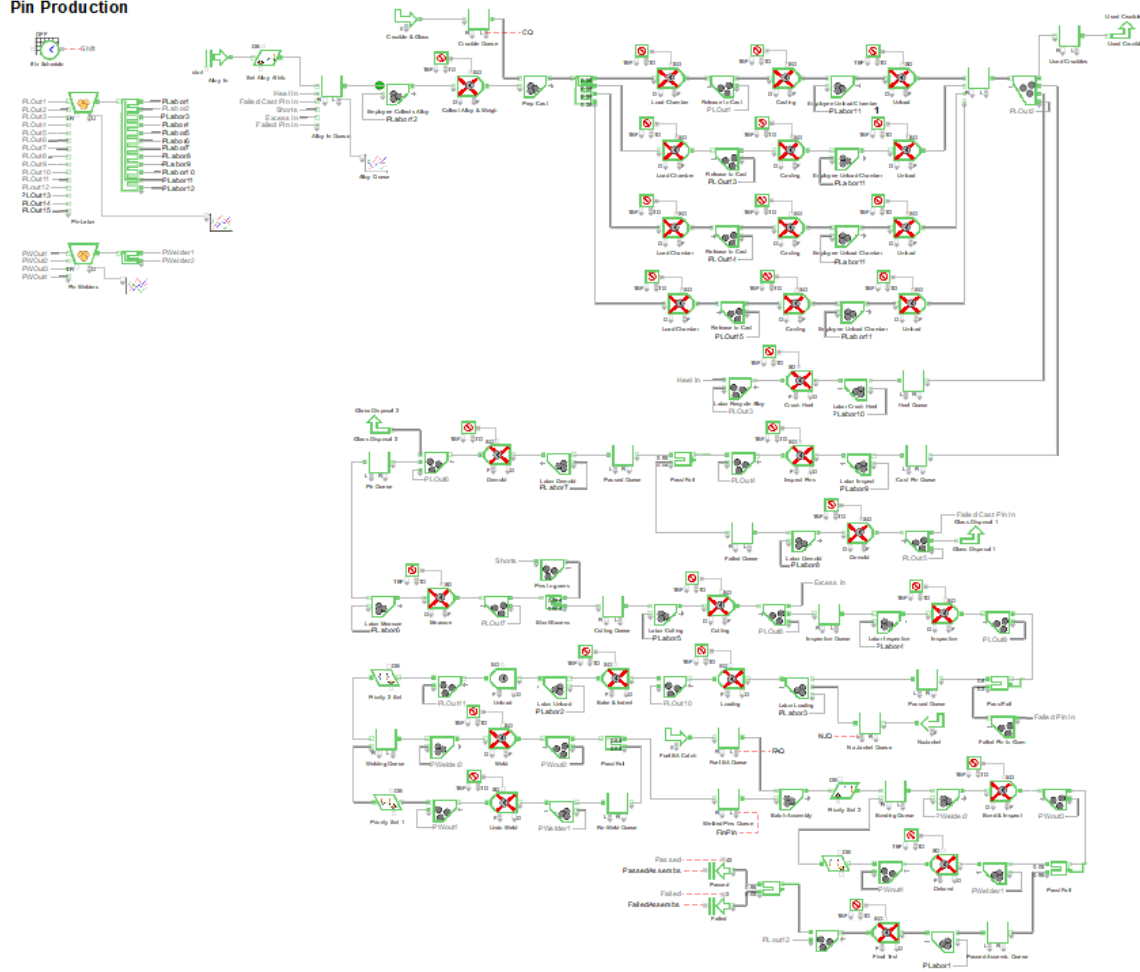
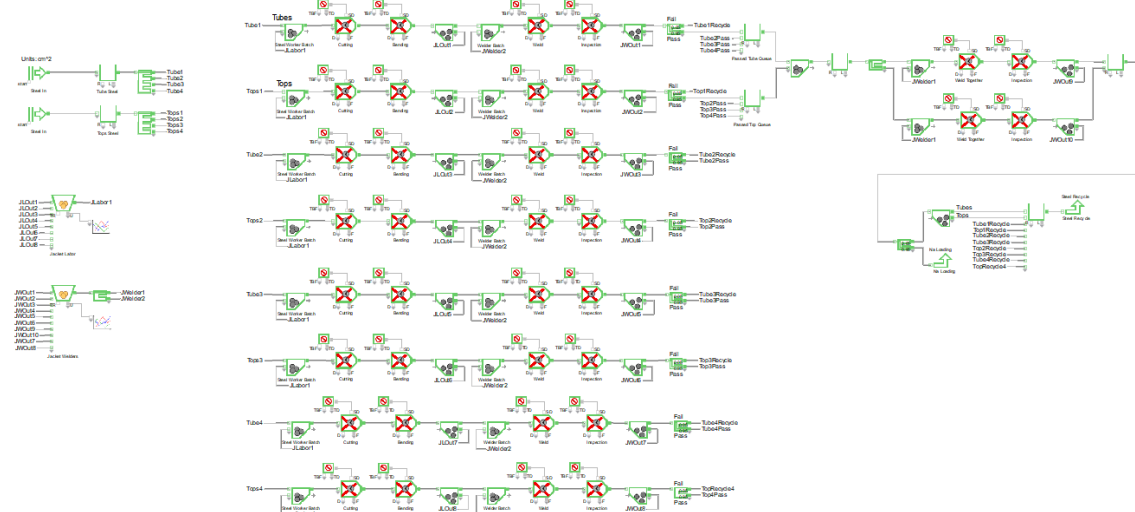Figure G.2: Pin production subsystem model for 4-10 work week scenarios
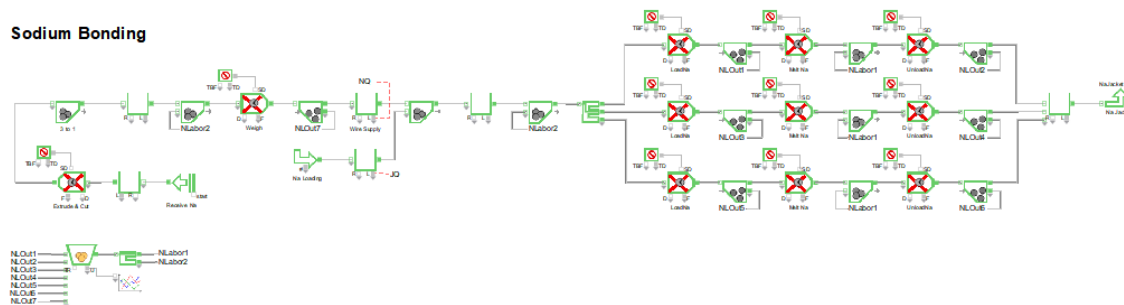
Figure G.3: Jacket production subsystem model.

Figure G.4: Sodium and sodium bonding subsystem model.
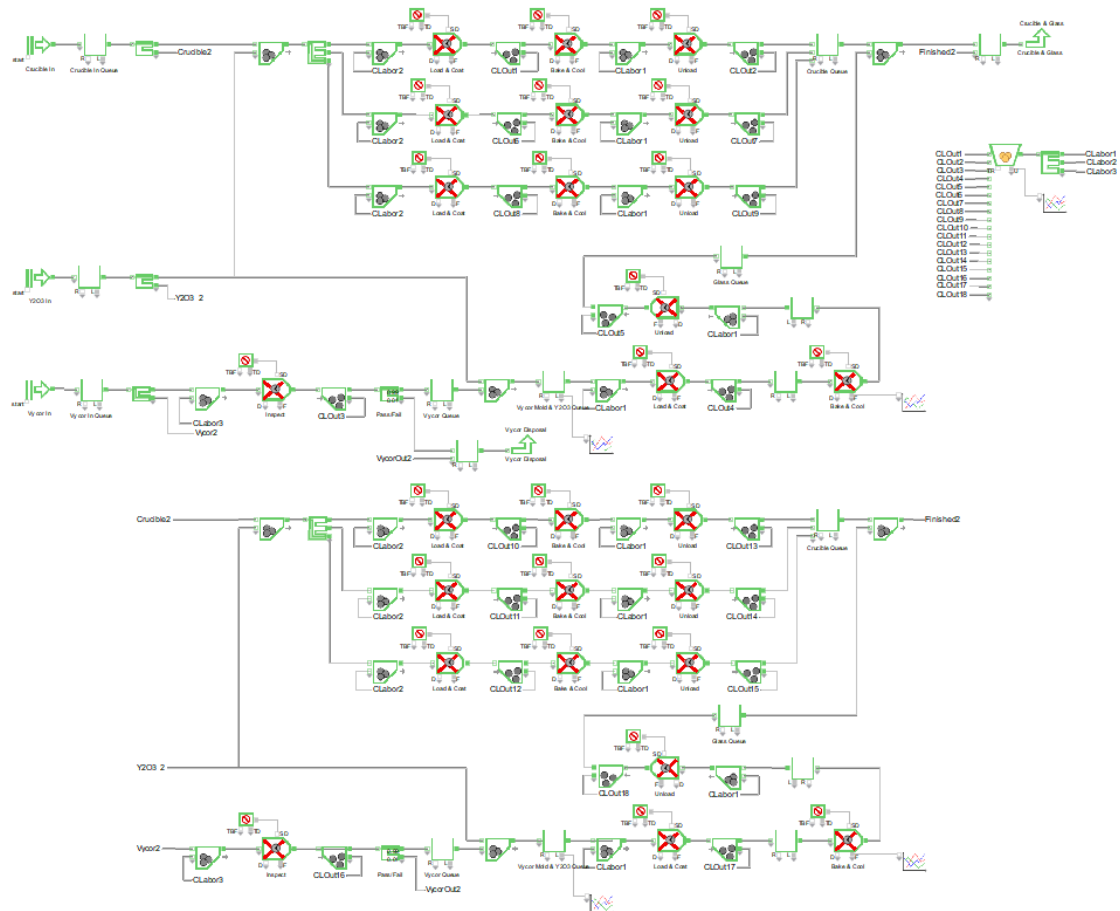
Molds (Vycor & Crucible) Production

Figure G.5: Crucible and molds production subsystem model.
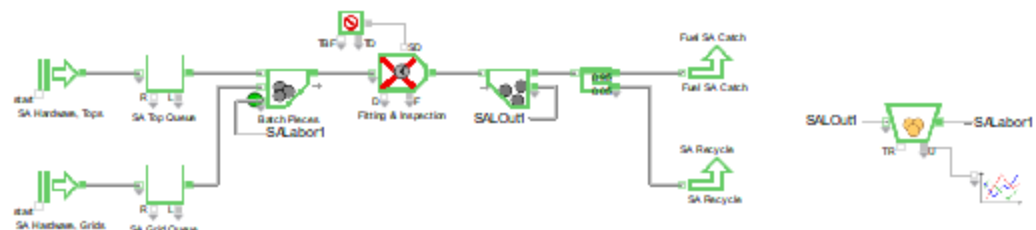
Fuel Sub-Assebmly Hardware

Figure G.6: Assembly hardware production model.
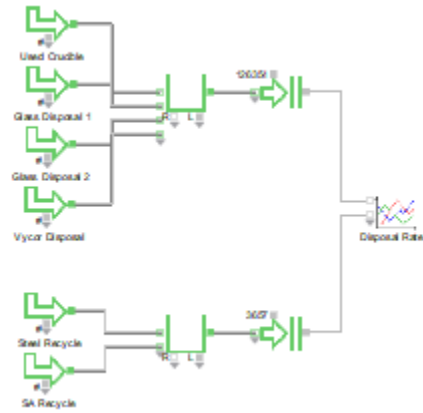
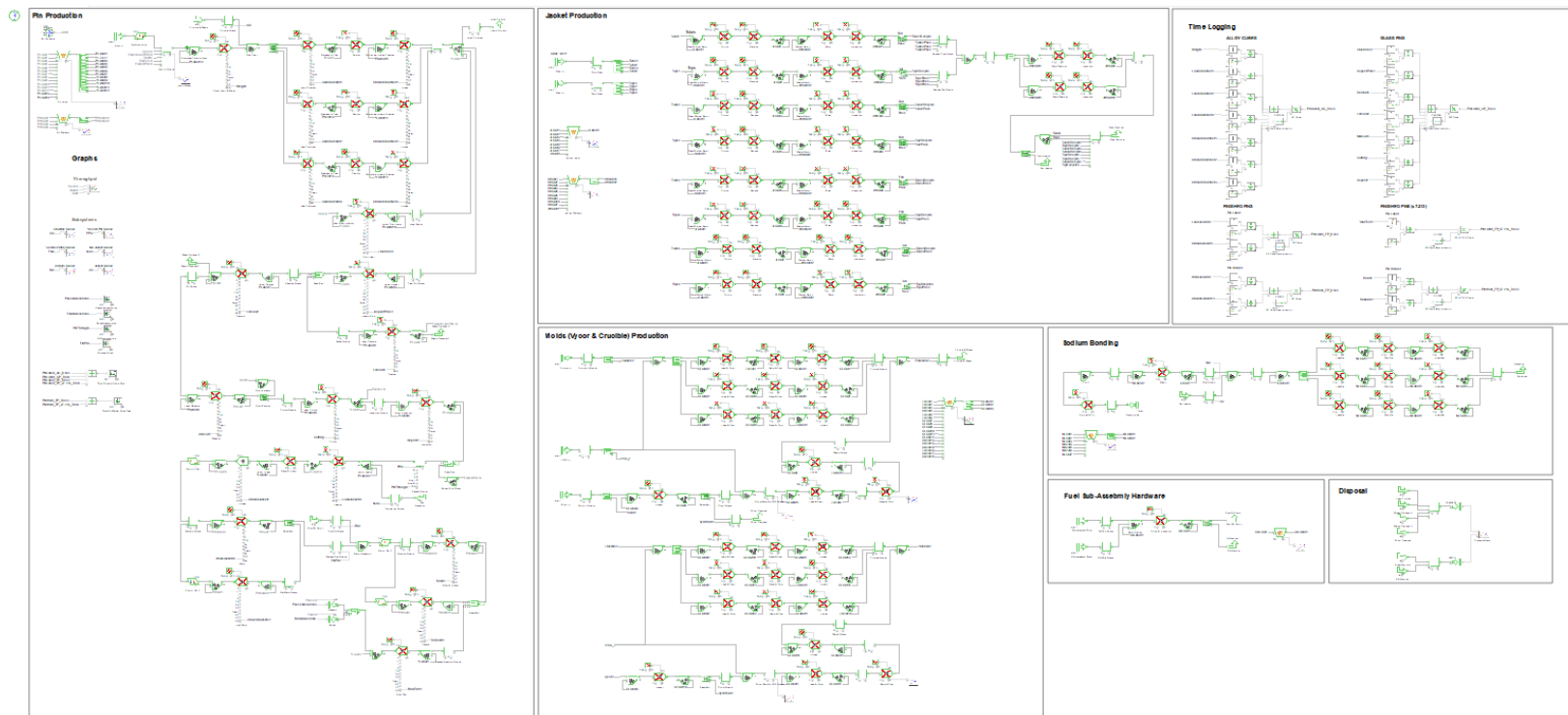Figure G.7: Waste byproduct disposal model.

Figure G.8.1:   Full model of 5-8 work week systems (Scenarios 1-3, 7, 9, 11, & 12).
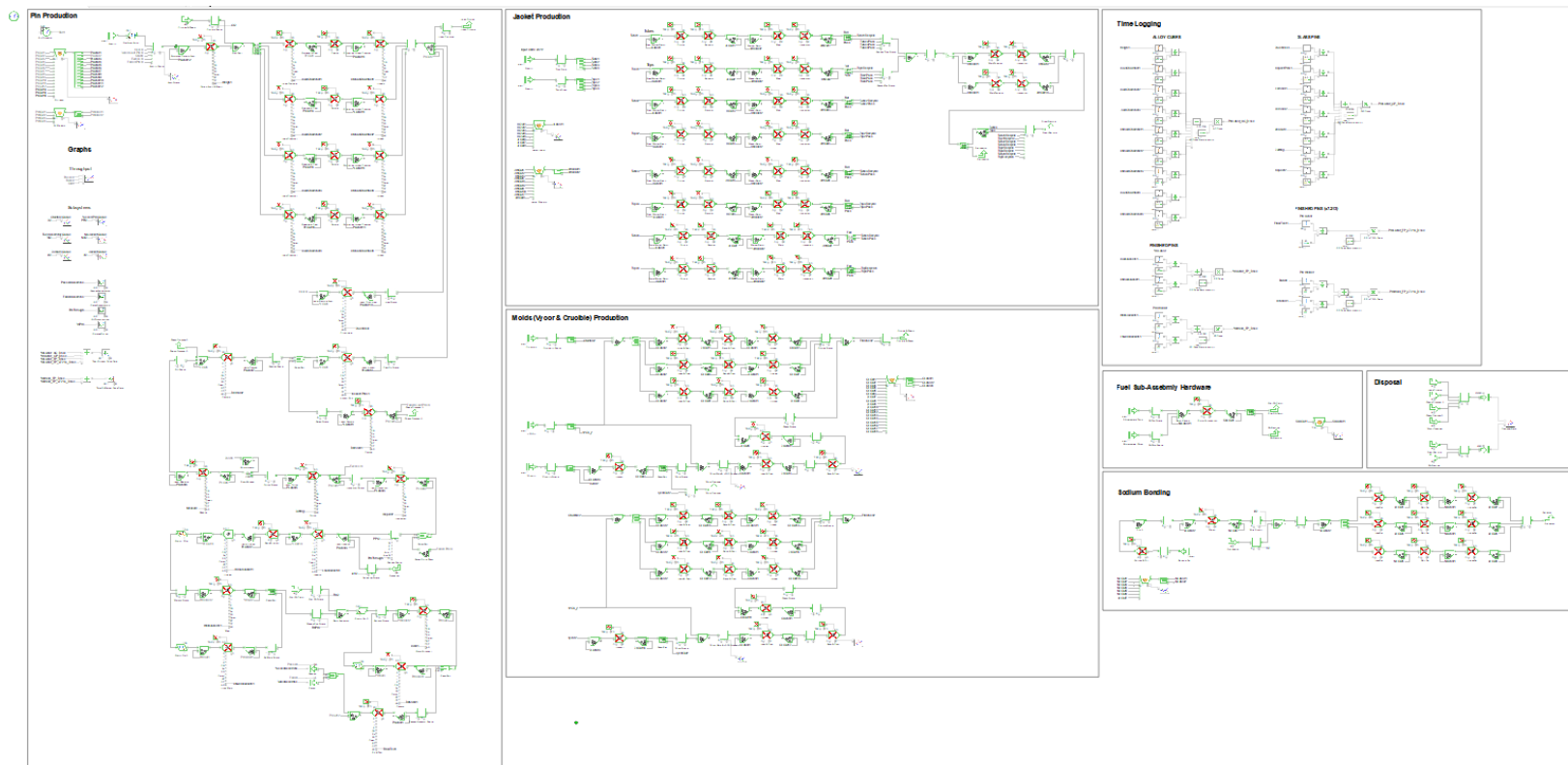
Figure G.8.2:   Full model of 4-10 work week systems (Scenarios 4-6, 8, & 10).

References

[1]   Pasamehmetoglu, K. (2019). Versatile Test Reactor Overview [Conference presentation]. Advanced Reactor Summit VI, San Diego, California, United States.

[2]   Crawford, D. C., Hayes, S. L., & Powers, J. J. (2018). *VTR Startup Fuel Paper for NFSM* (Report INL/EXT-18-44673-Revision-0). Idaho Falls, ID: Idaho National Laboratory.

[3]   Crawford, D. C (2018). Versatile Test Reactor Startup Fuel Update [PowerPoint slides].

[4]   Walters, L. C. (1998). Thirty years of fuels and materials information from EBR-II. *Journal of Nuclear Materials, 270*, 39-48. https://doi.org/10.1016/S0022-3115(98)00760-0

[5]   Crawford, D. C., Hayes, S. L., Powers, J. J., & Maloy, S. A. (2018). *A Proposed VTR Startup Fuel* [Conference presentation], Nuclear Fuels and Structural Materials American Nuclear Society Annual Meeting, Philadelphia, PA, United States.

[6]   Jones, C. G. (2005). A review of the history of U.S. radiation protection regulations, recommendations, and standards. *Health Physics, 88(2),* 105-124. https://doi.org/10.1097/01.HP.0000146629.45823.da

[7]   Hayes, S. L. (2010). *Basics of Nuclear Fuels* [Conference presentation], ATR-NSUF Users Week, Idaho Falls, ID, United States.

[8]   Chang, Y. I. (2007). Technical Rationale for Metal Fuel in Fast Reactors. *Nuclear Engineering and Technology, 39*(3), 161-170.

[9]   Fast Reactor Working Group (FRWG) (2018). Nuclear Metal Fuel: Characteristics, Design, Manufacturing, Testing, and Operating History.

[10]   Kim, J. H., Lee, J. W., Kim, K. H, & Park, J. Y. (2017). Injection casting of U-Zr and U-Zr-RE fuel slugs and their characterization. *Journal of Nuclear Science and Technology, 56*(6), 648-654. https://doi.org/10.1080/00223131.2017.1299049

[11]   Ogata, T. & Mizuno, T. (2009). *Directions of Metal Fuel Development for Fast Reactors* [Conference presentation], Proceedings of the GLOBAL 2009 congress – The Nuclear Fuel Cycle: Sustainable Options and Industrial Perspectives, Paris, France.

[12]   Walter, C. M., Golden, G. K., & Olson, N. J. (1975). *U-Zr-Pu Metal Alloy: A Potential Fuel for LMFBR's* (Report ANL-76-28). Argonne, IL: Argonne National Laboratory.

[13]   Burkes, D. E., Fielding, R. S., Porter, D. L., Crawford, D. C., & Meyer, M. K. (2009). A US perspective on fast reactor fuel fabrication technology and experience part I: metal fuels and assembly design. *Journal of Nuclear Materials, 389*, 458-469. https://doi.org/10.1016/j.jnucmat.2009.02.035

[14]   Werner, C. J. (2018). *MCNP6.2 Release Notes* (Report LA-UR-18-20808). Los Alamos, NM: Los Alamos National Laboratory.

[15]   Khintchine, A. (1929). Sur la loi des grands nombres [The law of large numbers]. *Comptes rendus de l'Académie des Sciences, 189,* 477-479.

[16]   Hammersley, J. & Handscomb, D. C. (1964). *Monte Carlo Methods*. London: Chapman and Hall.

[17]   Bielajew, A. F. (2001). Fundamentals of Monte Carlo methods for neutral and charged particle transport.

[18]   Shultis, J. K. & Faw, R. E. (2000). *Radiation Shielding*. La Grange Park, IL: American Nuclear Society, Inc.

[19]   Duderstadt, J. J. & Hamilton, L. J. (1976). *Nuclear Reactor Analysis*. Hoboken, NJ: John Wiley & Sons, Inc.

[20]   Brunner, T. A. (2002). *Forms of Approximate Radiation Transport* (Report SAND2002-1778). Albuquerque, NM: Sandia National Laboratories.

[21]   International Commission on Radiological Protection (ICRP) (2012). Compendium of Dose Coefficients Based on ICRP Publication 60. ICRP Publication 119. Ann. ICRP 41(suppl.).

[22]   Title 10, Volume 1, C.F.R. § 20.1003 (2008). https://www.nrc.gov/reading-rm/doc-collections/cfr/part020/part020-1003.html

[23]   Title 10, Volume 1, C.F.R. § 20.1201 (2006). https://www.nrc.gov/reading-rm/doc-collections/cfr/part020/part020-1201.html

[24]   Knief, R. A. (2008). *Nuclear Engineering Theory and Technology of Commercial Nuclear Power*. La Grange Park, IL: American Nuclear Society, Inc.

[25]   Oldenburg, O. & Rasmussen, N. C. (1966). *Modern Physics for Engineers*. New York City, NY: McGraw-Hill

[26] McLaughlin, T. P, Monahan, S. P., Pruvost, N. L., Frlov, V. V., Ryazanov, B. G., & Sviridov, V. I. (2000). *A Review of Criticality Accidents: 2000 Revision* (LA-13638). Los Alamos, NM: Los Alamos National Laboratory.

[27] Banks, J. (Ed.). (1998). *Handbook of simulation: Principles, methodology, advances, applications, and practice.* John Wiley & Sons, Inc.

[28] Tako, A. A. & Robinson, S. (2012). The application of discrete event simulation and system dynamics in the logistics and supply chain context. *Decision Support Systems, 52(4)*, 802-815. https://doi.org/10.1016/j.dss.2011.11.015

[29] Brailsford, S. C. & Hilton, N. A. (2001). *A comparison of discrete event simulation and system dynamics for modelling health care systems*.

[30] Cornuejols, G. & Tütüncü, R. (2006). Optimization Methods in Finance. London, GB: Cambridge University Press.

[31] Negahban, A. & Smith, J. S. (2013). Simulation for manufacturing system design and operation: Literature review and analysis. *Journal of Manufacturing Systems*, *33(2)*, 241-261. https://doi.org/10.1016/j.jmsy.2013.12.007

[32] Sackett, C., Diamond, P., & Hansen, K. (2017). *ExtendSim 9 User Guide.*

[33] Rearden, B. T. & Jessee, M. A. (2016). SCALE Code System, ORNL/TM-2005/39, Version 6.2 [Computer software].Oak Ridge, TN: Oak Ridge National Laboratory. Available from Radiation Safety Information Computational Center as CCC-834.

[34] Imagine That Inc. (2018). ExtendSim Pro 10 [Computer software]. San Jose, California.

[35] Hermann, O. W., Renier, J. P., & Parks, C. V. (1994). *Technical Support for a Proposed Decay Heat Guide Using SAS2H/ORIGEN-S Data. NUREG/CR-5625* (Report ORNL-6698). Oak Ridge, TN: Oak Ridge National Laboratory.

[36] Schwarz Software & Consulting, LLC (2011). MCNPX Visual Editor (*Ver. 2.7.E.*) [Computer software].

[37] Goorley, T. (2008). *MCNP Medical Physics Geometry Database. Los Alamos National Laboratory* (Report LA-UR-08-2468).

[38] Idaho National Laboratory (INL) (n.d.). *Special Nuclear Materials Glovebox*. Retrieved from https://mfc.inl.gov/SitePages/Instruments/Fuel%20Manufacturing%20Facility/Special%20nuclear%20materials%20glovebox.aspx

[39]   Rao, N., Hagemeyer, D. A., & Holcomb, D. B. (2017). *Occupational Radiation Exposure Report for Calendar Year 2018*. Retrieved from https://energy.gov/ehss/occupational-radiation-exposure

[40]   Bertsimas, D. & Tsitsiklis, J. N. (1997). *Introduction to Linear Optimization*. Nashua, NH: Athena Scientific.

[41]   Jelinek, H. F., Carson, N. J., Jr., & Shuck, A. B. (1962). *Fabrication of EBR-II, Core-I fuel pins* (ANL-6274). Argonne, IL: Argonne National Laboratory.

[42]   Cameron, T. C. & Hessler, N. F. (1961). *Assembling, sodium bonding and bond testing of EBR-II fuel rods* (ANL-FGF-276). Argonne, IL: Argonne National Laboratory.

[43]   Lacksonen, T. (2001). Empirical comparison of search algorithms for discrete event simulation. *Computers & Industrial Engineering, 40*, 133-148. https://doi.org/10.1016/S0360-8352(01)00013-4

[44]   Buchholz, P. (2009). Optimization of stochastic discrete event simulation models. *Models and Algorithms for Optimization in Logistics*.

[45]   Riley, L. A. (2013). Discrete-event simulation optimization: a review of past approaches and propositions for future direction. *Proceedings of the 2013 Summer Computer Simulation Conference, 47*.

[46]   Kornreich, D. (2020). Representative glove box prices [personal communication].

[47]   International Atomic Energy Agency (IAEA). (2010). *Cost aspects of the research reactor fuel cycle* (No. NG-T-4.3). Vienna, Austria.

[48]   Parga, J. R., Jr. (2017). Constrained black box optimization for radioisotope thermal generator manufacturing [Master's thesis, The University of Texas at Austin]. Texas ScholarWorks.

[49]   Hezir, J. S. (2015). Perspectives on National Laboratory Cost Accounting Issues: Commission to review the effectiveness of the national energy laboratories.

[50]   Neimeier, H. (1996). Analytic uncertainty modeling versus discrete event simulation. *PHALANX, March*.

[51]   Brookhaven National Laboratory (2020). *NuDat 2* [Data set]. National Nuclear Data Center. http://www.nndc.bnl.gov/nudat2